



Mechanism of short pitch rail corrugation: initial excitation and frequency selection for consistent initiation and growth

Zili Li, Shaoguang Li, Pan Zhang, Alfredo Núñez & Rolf Dollevoet

To cite this article: Zili Li, Shaoguang Li, Pan Zhang, Alfredo Núñez & Rolf Dollevoet (2022): Mechanism of short pitch rail corrugation: initial excitation and frequency selection for consistent initiation and growth, International Journal of Rail Transportation, DOI: [10.1080/23248378.2022.2156402](https://doi.org/10.1080/23248378.2022.2156402)

To link to this article: <https://doi.org/10.1080/23248378.2022.2156402>



© 2022 The Author(s). Published by Informa UK Limited, trading as Taylor & Francis Group.



Published online: 16 Dec 2022.



Submit your article to this journal [↗](#)



View related articles [↗](#)



View Crossmark data [↗](#)

Mechanism of short pitch rail corrugation: initial excitation and frequency selection for consistent initiation and growth

Zili Li, Shaoguang Li, Pan Zhang, Alfredo Núñez and Rolf Dollevoet

Section of Railway Engineering, Delft University of Technology, Delft, The Netherlands

ABSTRACT

This paper proposes a new hypothesis for the formation process of short pitch rail corrugation. An FE wheel-track dynamic model is utilized to verify the hypothesis by reproducing corrugation initiation and consistent growth. It is found longitudinal compression modes are responsible for corrugation initiation with necessary initial excitation that allows flexibility for longitudinal vibration. Consistency between longitudinal compression and vertical bending eigenfrequencies of the wheel-track system is required for consistent corrugation growth, which also determines maximum corrugation amplitude. Corrugation initiates by frequency selection instead of wavelength fixing. The proposed mechanism can explain field observations including the wavelength and periodicity of corrugation in the Netherlands, why corrugation forms on continuously-supported tracks where pinned-pinned resonance does not exist, and the small variation between the corrugation wavelength and train speed.

ARTICLE HISTORY

Received 29 September 2022

Revised 3 December 2022

Accepted 4 December 2022

KEYWORDS

Short pitch rail corrugation; consistent initiation and growth; initial excitation; rail longitudinal compression vibrations; frequency selection; wavelength fixing



1. Introduction

1.1. Literature review

Rail corrugation has been known and investigated for more than one century [1]. There have been extensive experimental investigations [2–6], metallurgical characterization of the rail surface material microstructural changes [7–11], and analytical and numerical studies [12–20]. Some other research publications can be found in the review papers [1,21,22]. Grassie and Kalousek [1] classified corrugation into six different groups based on damage mechanisms and wavelength-fixing mechanisms, i.e. heavy haul, light rail, booted sleeper, contact fatigue, rutting and short pitch corrugation. Short pitch corrugation, also known as ‘roaring rail’ due to the noise radiation it produces [23,24], has the following characteristics [1]: 1) its wavelength falls in the range of 20–80 mm, and its amplitude can be up to 100 μm ; 2) it predominantly occurs on straight tracks or at gentle curves; and 3) field data show that the wavelength is insensitive to train speed [1,15,25]. While most groups of corrugation have been well understood in the literature, the formation mechanism of short pitch corrugation remains unclear [15,26]. In the remainder of this paper, the term ‘corrugation’ refers to short pitch corrugation.

Currently, corrugation formation is explained by a process including structural dynamics and a damage mechanism [26–28]. The structural dynamics determines the corrugation wavelength, and the main damage mechanism is usually considered to be differential wear [29–33].

Corrugation is a complex problem principally due to its unknown wavelength-fixing mechanism. In the literature, different hypotheses have been proposed for this mechanism. They

CONTACT Zili Li  z.li@tudelft.nl  Section of Railway Engineering, Delft University of Technology, Stevinweg 1, Delft, CN 2628, The Netherlands

considered either the instability of wheel-rail systems or structural dynamics. The instability of wheel-rail systems relates corrugation to stick-slip vibrations [18,34,35]. Stick-slip vibrations are induced by negative friction under saturated creep conditions [36] and do not apply to the corrugation on straight tracks or at gentle curves with relatively low tractions. The hypotheses about structural dynamics include factors such as the P2 resonance (the unsprung mass vibrating on the track stiffness) at approximately 50 ~ 100 Hz [15,37], the sleeper passing frequency [38,39], the wheelset second torsional resonances at 250 ~ 400 Hz [19,27,40], and the ‘pinned-pinned’ resonance at 400 ~ 1200 Hz, where the wavelength equals twice the sleeper span [27,41].

For the frequency range of interest of the corrugation at high speed, the ‘pinned-pinned’ resonance is widely considered the wavelength-fixing mechanism. Therefore, short pitch corrugation is also named ‘pinned-pinned resonance’ corrugation [27]. The hypothesis built upon the ‘pinned-pinned’ resonance is frequency fixing instead of wavelength fixing [42]. According to the frequency-fixing mechanism, the corrugation wavelength should increase linearly with train speed. However, field data show that corrugation is insensitive to train speed variations [1,15,25]. This disagreement was explained in [42], by proposing that the corrugation was formed by different wavelength-fixing mechanisms, i.e. pinned-pinned resonance is not the only wavelength-fixing mechanism. In addition, the ‘pinned-pinned’ resonance cannot sufficiently explain corrugation for the following reasons: 1) corrugation can also form on continuously supported tracks despite much smaller occurrence probability where pinned-pinned resonance does not exist [22,43]; 2) the corrugation formed on Vancouver ‘Skytrain’ shows no influence by different sleeper supporting spans [25]; and 3) field data regarding the small variation between the corrugation wavelength and train speed from British Rail Research and Cambridge University cannot be explained [1,15,25].

To understand the wavelength-fixing mechanism, the significance of contact mechanics was also addressed. To explain why corrugations are observed only in the range of 20–80 mm, a contact filtering effect was proposed [12,33,44]. The contact filter guarantees that only corrugations falling in the short pitch range can grow. Then, the wavelength-fixing mechanism is explained as certain structural dynamics causing differential wear with their corresponding wavelengths falling into the amplification zone determined by the contact filter [12].

Many models have been developed to understand corrugation formation mechanisms, such as multibody models [45,46], beam models [47–49], and finite element models [26,50,51]. In addition to linear contact mechanics models, the more complex non-Hertzian [33] and nonsteady state [28,52,53] treatments of wheel-rail contact mechanics were included. Models with those more complex features are expected to be more accurate; however, they have reported no corrugation growth [26,52,54]. Therefore, the formation mechanism of corrugation remains elusive.

1.2. Problem statement: initial excitation and mechanism of frequency selection for consistent initiation and growth

In this work, we introduce two necessary conditions for corrugation continuous initiation and growth motivated by the vast previous research and the corrugation-like waves often observed after rail squats [55,56]. In [26], the first necessary condition was proposed that rail longitudinal vibration modes are probably dominant for corrugation initiation and that for continuous corrugation initiation and growth, there should be a consistency among the vertical and longitudinal vibration modes, the dynamical responses and the resulting wear.

In this paper, we first propose the second necessary condition for corrugation initiation – the initial excitation. We then show that with a proper initial excitation, the wheel-track system selects to resonate around a longitudinal central frequency so that the corrugation can indeed initiate and grow consistently, and thus continuously, with a seemingly ‘fixed’ wavelength. Such excitation is called effective initial excitation.

Generally, for the initiation of dynamics-induced rail rolling contact failures, there should be an initial excitation to the system. With this initial excitation, dynamic wheel-rail contact forces are

generated in certain wavelength ranges, and result in differential wear and differential plastic deformation. After many wheel passages, defects form due to the accumulation of wear and plastic deformation [57]. In the case of corrugation, the initial excitation can be local geometrical irregularities (e.g. squats [36] and scratches [58]), local material irregularities (inhomogeneity) and the associated geometrical irregularities (e.g. poor welds [59]), and anomalies that are often invisible in track systems. An important feature of the corrugation induced by local irregularities is that the local irregularities are often visible; they excite large vertical vibrations, and the resulting corrugation-like waves usually decay over a finite number of wavelengths. In contrast, corrugation with invisible initial excitation often appears over a much longer distance. These results suggest that local vertical excitation is not the cause of the latter corrugation.

This paper focuses on invisible excitation. The results in [26,52,54] give reasonable explanations regarding why track systems with nominal parameters can be corrugation-free, in agreement with field observations that corrugation appears on some types of tracks in some circumstances and not in others [42]. This means that such nominal parameters, including the associated modelling, do not include effective initial excitations. There have been some studies on the corrugation problem from the viewpoint of fastenings (including railpads) [17,51,60,61]. Field data show that fastening systems are influential in corrugation formation [5,26]. However, track parameters, such as those of fastenings, that possibly introduce an effective initial excitation to the vehicle-track system are still to be investigated and identified. An effective initial excitation should initiate the fluctuations of wheel-rail contact forces, cause differential wear or deformation, and finally lead to consistent corrugation formation, i.e. initiation and growth.

In this paper, we hypothesize a corrugation formation process and investigate whether effective *initial excitations* and the necessary *consistency* can be achieved by controlling certain fastening parameters and how a central frequency is selected that leads to an apparent fixed wavelength. A 3D transient finite element (FE) vehicle-track interaction model with frictional rolling contact [26,59,62,63] is employed to simulate the hypothesized corrugation formation process. Here, fastening parameters mean both the choice of the parameters and the modelling of the fastening.

1.3. Structure of this paper

The paper is organized as follows. A hypothesis for a consistent corrugation initiation and growth process is proposed in Section 2. Section 3 introduces the models employed to verify the hypothesis of Section 2. In Section 4, corrugation initiation from an initial excitation determined by fastening modelling is presented. It is further shown that rail longitudinal compression modes cause corrugation initiation. Section 5 studies the corrugation growth from the corrugation initiated in Section 4. The consistency condition for continuous corrugation initiation and growth is analysed by examining the behaviour of the differential wear W_f in relation to the longitudinal and vertical contact forces F_L and F_N . Section 6 continues to study the roles of the eigenfrequencies, and a mechanism of frequency selection is identified that ‘fixes’ the apparent wavelength in a seemingly speed-independent manner. Finally, in Section 7, conclusions and further work are summarized.

2. Hypothesis for a consistent corrugation initiation and growth process

Based on [26], a process of consistent corrugation initiation and growth is hypothesized and shown in Figure 1a. This process contains four steps.

Step (a) Initial excitation: The rail is smooth in the beginning. When a wheel rolls over the track with an initial excitation, dynamic responses of the track are induced, dynamic contact forces arise, and the resulting initial differential wear of certain wavelengths is obtained through FE simulation. This wear causes the very initial corrugation after the first wheel passage, whose severity is quantified with a maximal peak-to-trough distance $(2A_{\max})_0$. The initial excitation will be discussed in Section 4.1.

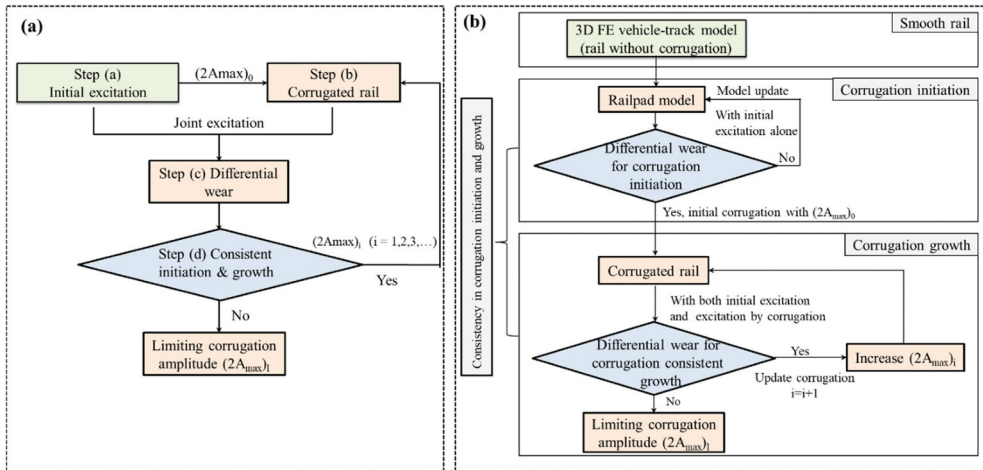


Figure 1. The hypothesis for consistent initiation and growth of the corrugation. (a) the flowchart of the hypothesis; (b) the flowchart of the computer simulation that examines the hypothesis. Step (a) is examined in Section 4, and the remainder is analyzed in Section 5.

Step (b) Corrugated rail: After the first wheel passages on the smooth rail, the initial corrugation of $(2A_{\max})_0$ will develop and is thus applied to the rail surface. It is proportional to and in antiphase with the initial differential wear. Antiphase means a wear peak causes a corrugation trough. Similarly, additional wear from Step (d) is added to the corrugation to become $(2A_{\max})_i$ ($i = 1, 2, 3, \dots$) to simulate subsequent wheel passages.

Step (c) Differential wear by the joint excitation of the initial excitation and the corrugated rail: The rail is now corrugated, which can be in its initial form of $(2A_{\max})_0$, as shown in Step (a), or a more advanced form of $(2A_{\max})_i$ ($i = 1, 2, 3, \dots$), as shown in Step (b). The corrugation is an additional excitation besides the initial excitation. Both excitations can cause differential wear of their respective wavelengths.

Step (d) Consistency of the differential wear: The growth of the corrugation will be determined jointly by the wear caused by the two excitations. For consistent initiation and growth, the wear must add up to each other so that $(2A_{\max})_i > (2A_{\max})_{i-1}$. This requires that the phase and wavelength of the wear remain the same or at least sufficiently close to each other. This is the *consistency condition*. The corrugation will continuously grow when the consistency condition is met.

Now let the wheel roll over the corrugated rail, calculate the differential wear and check if the consistency condition is satisfied. If the condition is satisfied, then repeat Steps (b), (c), and (d) with increased $(2A_{\max})_i$ until a limiting $(2A_{\max})_l$, with which the condition is no longer satisfied (see Figure 1(b)). It will be shown in this paper that with a certain given set of fastening parameters (e.g., RPM3), corrugation initiates and grows consistently from the smooth rail to the corrugated rail with amplitudes up to $80 \mu\text{m}$, i.e. $(2A_{\max})_l = 80 \mu\text{m}$. If the condition is not satisfied, then the given set of parameters is not suitable for further growth of the corrugation. Alternatively, it can mean that the damage mechanism is not differential wear (anymore) but, e.g., (differential) plastic deformation. A further search for more sets of suitable parameters and the consideration of a different damage mechanism, such as plastic deformation, are beyond the scope of this paper.

3. Numerical models

3.1. FE model

The model should consider the structural dynamics, the mechanics of wheel-rail contact that couples the vehicle with the track where the corrugation takes place, and the damage mechanism.

A 3D FE vehicle-track model was developed as shown in Figure 2. The model is based on a symmetrical vehicle-track system of a straight track. Thus, a half-track and a half wheelset are considered. The car body and bogie structures above the primary suspension are lumped into a mass, which usually influence the vehicle-track dynamic interaction in the relatively low-frequency range (tens of Hz [64]), beyond the relevant frequency range of corrugation. This simplification does not consider the effect of the bogie flexibility and the multiple bogie wheelsets, which play an important role in high-frequency vehicle-track interaction [20,65] and will be further studied in future work. Spring-damper elements represent the primary suspension. The wheelset, rail, and sleepers are modelled with 3D finite elements. The radius of the wheel is 460 mm, with a conicity of 1/40. The rail is UIC 54 with a 1/40 inclination. Fastenings and ballast are also modelled as spring-damper elements. Track parameters representing the typical Dutch railway system are referenced from [26,66]. The solution zone with a meshing size of 0.8 mm starts at 0.3 m from the initial wheel location. The track length is 20.54 m and non-reflecting boundary conditions have been applied to two rail ends. The wheel-rail interaction is treated as surface-to-surface contact with a penalty method [67]. Coulomb's frictional law is applied, with the friction coefficient being 0.4. The longitudinal load is defined with a traction coefficient of $\mu = 0.15$. The running speed is 140 km/h. In the simulations, an implicit-explicit sequential approach is employed [62,63]. The time step in the explicit integration is 4.67×10^{-8} s, which is small enough to meet the Courant stability condition [68]. Because of the nature of the explicit integration, the transient rolling contact and high-frequency dynamics of the wheel-track system are automatically included in the solution [63].

The dynamic interaction between them is through wheel-rail frictional rolling. This model has been verified by comparison with the established Hertz, Spence, Cataneo, Mindlin, and Kalker contact solutions [62,69]. Its ability to represent the wheel-track structural dynamics has been shown with hammer tests [70] and axle-box acceleration measurements [71]. The model includes direct coupling between the contact mechanics and the structural dynamics; this renders it able to explain problems arising from dynamic vehicle-track interactions, such as rail squat development and corrugation-like waves induced by squats [55,59,66,72]. As noted in [73], the model 'provides a very good explanation for the development of corrugation initiated from isolated railhead irregularities.' Furthermore, the model was used in [26] to study corrugation, with new insights gained about the conditions for corrugation initiation and growth, although corrugation growth

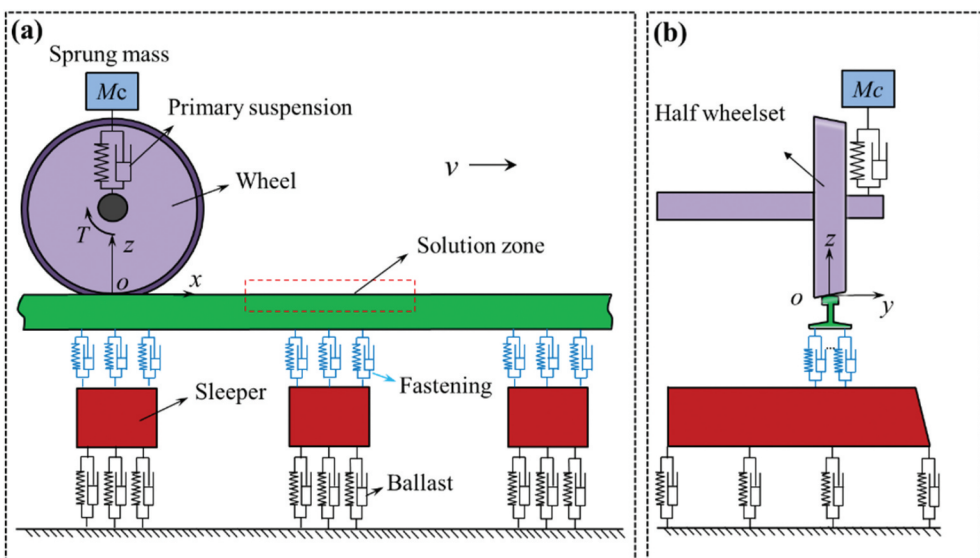


Figure 2. Schematic diagram of the FE vehicle-track model. (a) front view; (b) side view.

was not numerically reproduced there. Then, using the results in [26], this present paper further investigates the mechanism for consistent initiation and growth of corrugation.

3.2. Fastening models

Figure 3 shows the modelling of a fastening in the FE vehicle-track model, representing the nominal track situation (RPM1 in Figure 3b). The fastening is represented with 4×3 columns and rows of spring-damper elements and constrains the rail in the longitudinal (x), lateral (y), and vertical (z) directions. Due to the degradation of fastening, e.g., by wear of the railpad and clips, the rail may not necessarily be in uniform contact with the railpads and hence not be uniformly constrained. Thus, the constraining conditions in the model should take this into account. Different configurations of the spring-dampers with various constraining conditions can be defined with different fastening models. The influences of fastening modelling on the vertical and longitudinal contact forces excited by rail squats were studied by Zhao *et al.* [74]. It was identified that fastening modelling plays an important role in high-frequency vehicle-track interactions. Since there is a certain relationship between squats and corrugation [55], the effects of fastening models are also studied in this paper.

To investigate the effects of fastenings on corrugation initiation, five fastening models (RPM¹) are designed, as shown in Table 1. The five models are described with 3 terms in the 1st column, the first describing the vertical constraint of the rail nodes by fastenings, the second and third describing the constraint in the longitudinal and lateral directions, respectively. To clearly see the difference between the five models, symbols such as V-∞-4 are shown for each of the models in the 1st column. The meaning of the symbols can be found in the second column. For example, V-∞-4 means that the fastening has nominal railpad stiffness in the vertical direction (V), is continuously and rigidly constrained at all the

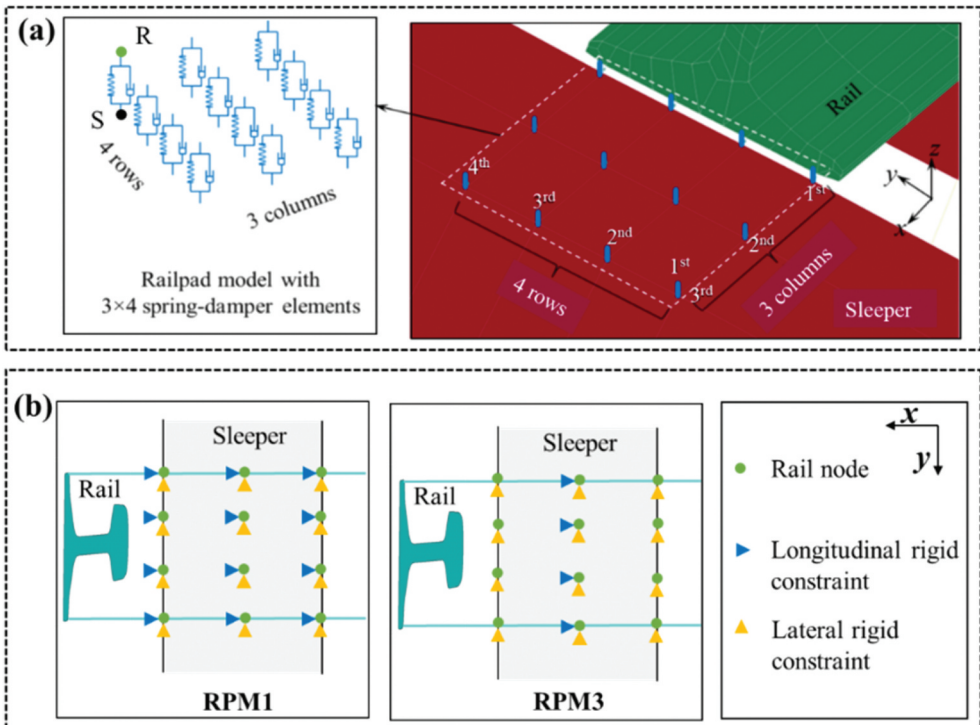


Figure 3. Fastening models of RPM1 and RPM3. (a) RPM1 that does not give rise to corrugation in [26]. (b) RPM3 that gives rise to corrugation in this paper.

Table 1. Five fastening models to understand corrugation initiation.

Fastening model	Description of the rail foot constraints	Purpose	Results
RPM1 (V-3-4)	Vertical: railpad stiffness ^a . Longitudinal: discretely & rigidly constrained at all the 3 columns. Lateral: discretely & rigidly constrained ^b at all 4 rows.	1. To model a nominal track. 2. To relate to [26] and as a reference to show a fastening model that does not cause corrugation.	It does not cause corrugation because of the strong longitudinal constraint so that the PSDs of W_f , F_L and displacement are low (Figures 4b, 7 and 9).
RPM2 (V-∞-4)	Vertical: as RPM1. Longitudinal: continuously ^c & rigidly constrained at all the nodes of the rail foot. Lateral: as RPM1.	To show no longitudinal compression modes, no corrugation.	It does not cause corrugation because of the strong longitudinal constraint so that the PSDs of F_L and displacement are low (Figures 6 and 9).
RPM3 (V-1-4)	Vertical: as RPM1. Longitudinal: discretely & rigidly constrained ^d at only 1 column (the middle column). Lateral: as RPM1.	To show a fastening model that gives the initial excitation and causes consistent initiation and growth of the corrugation.	It causes corrugation.
RPM4 (∞-1-4)	Vertical: continuously & rigidly constrained at all the nodes of the rail foot. Longitudinal: as RPM3 Lateral: as RPM1.	To show that corrugation occurs without rail vertical bending.	It causes corrugation.
RPM5 (∞-∞-4)	Vertical: as RPM4. Longitudinal: as RPM2. Lateral: as RPM1.	To show that rail longitudinal sheared vibration does not cause corrugation.	It does not cause corrugation because of the same rigid longitudinal constraint as RPM2.

a: The constraint has the nominal vertical stiffness of a railpad. b: as shown in Figure 3b. c: being continuously constrained means all the nodes at the rail bottom are constrained to the coordinate system. d: as shown in Figure 3b.

nodes of the rail foot in the longitudinal direction (∞) and is discretely and rigidly constrained with 4 rows of springs in the lateral direction (4). The lateral constraint of rail nodes in these five models keep the same, as shown in Figure 3(b) and Table 1.

RPM1 is employed in Section 4 to show a fastening model that does not give rise to corrugation, as presented in [26]. RPM3 (see Figure 3b) is used in Sections 4 and 5 to investigate the consistent initiation and growth of corrugation. RPM2, RPM4, and RPM5 are introduced in Section 4 to show, compared to RPM3, which structural dynamics are dominant for corrugation initiation.

3.3. Wear model

The damage by wear W_f at a point in the rail surface is assumed to be proportional to the accumulated frictional work done during wheel passages [13,52,75]. When such a point is represented by a surface element, the frictional work is calculated for each wheel passage, i.e. from the element entering until leaving the contact patch, as follows:

$$W_f(x, y) = kW_f(x, y) = k \sum_{i=1}^N \tau_i(x, y) v_i(x, y) \Delta t \quad (1)$$

where k is the wear coefficient, $w_f(x, y)$ is the frictional work, $\tau_i(x, y)$ and $v_i(x, y)$ are the local tangential stress and slip, respectively, and N is the number of time steps Δt during which the element passes through the contact patch.

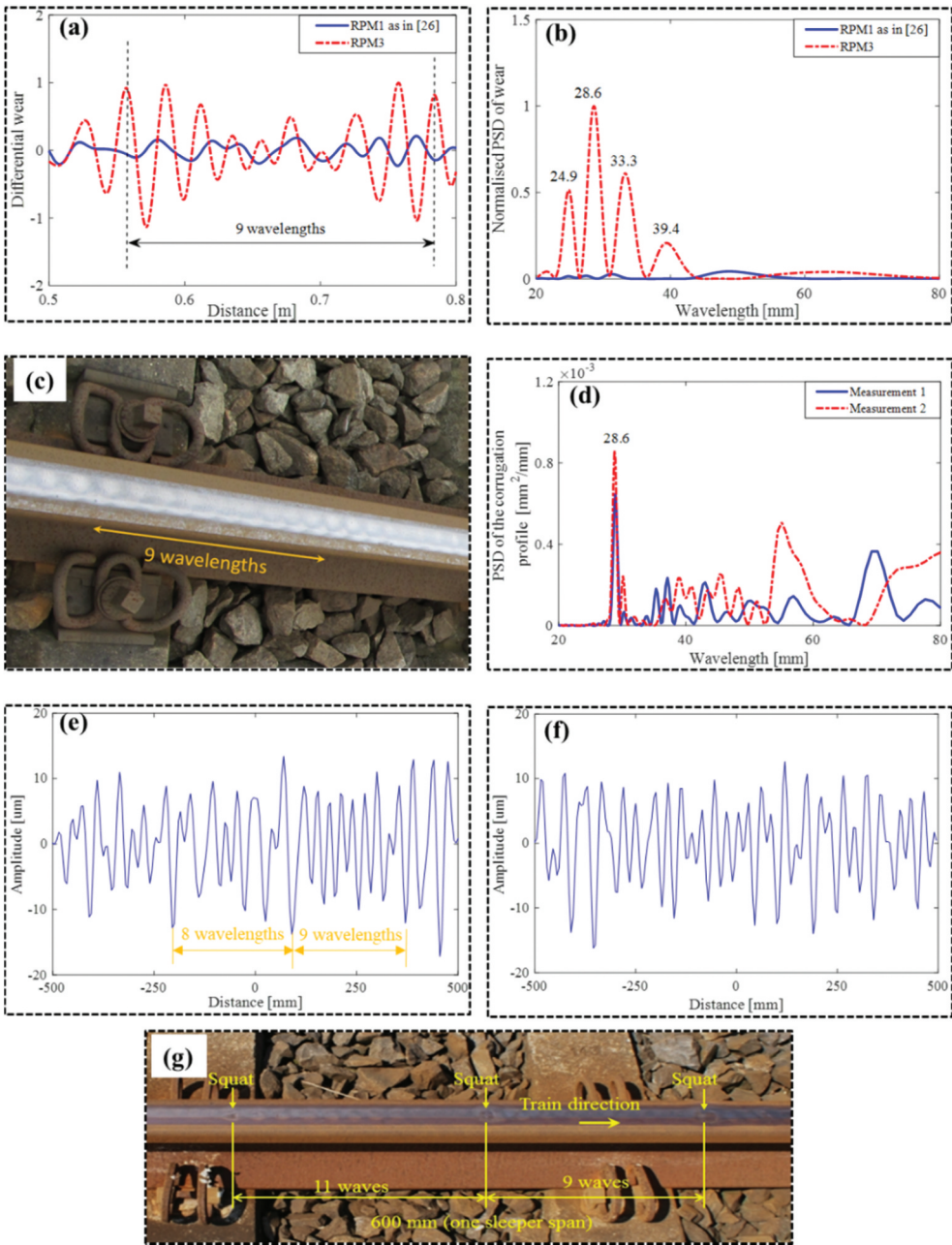


Figure 4. Initial differential wear W_f calculated with RPM1 and RPM3, 20–80 mm bandpass filtered. (a) in the spatial domain (the differential wear is normalized with the maximum amplitude of the differential wear under RPM3) and (b) in the wavelength domain (the PSD is normalized with the magnitude of the dominant wavelength component under RPM3). (c) Corrugation on a ballast track with mono-block sleepers and fastenings with a W-shaped tension clamp. It was on a straight track near Assen, the Netherlands. The corrugation amplitude was nonuniform. (d) PSD of 2 field corrugation measurements and (e) and (f) the 2 measurements of corrugation with PSD shown in (d). The corrugation was measured with RAILPROF over 1 meter with a 5 mm sampling interval along the middle of the rail top surface. (g) squats caused by corrugation, Deenik clips, track located in Steenwijk, the Netherlands (Source [26]).

4. Corrugation initiation

This section discusses corrugation initiation due to differential wear caused by an initial excitation, i.e. Step (a) of the hypothesized process of Section 2.

4.1. The initial excitation

First, the initial excitation is identified. In the literature, the differential wear is found to be sensitive to fastenings from both field observations and numerical modelling [5,26,74]. In [26], a fastening boundary condition corresponding to RPM1 was used, as shown in Figure 3b, and it was concluded that corrugation would not form. Through parametric variation studies, it was observed in the current study that in some situations, the differential wear has a higher power intensity in the corrugation wavelength range of 20–80 mm. One such situation, RPM3 (Figure 3b), is that in comparison to RPM1, the fastening longitudinal rigid constraints are released in the first and third columns and maintained only in the second column. In this case, a high amplitude of differential wear with wavelength components in the corrugation wavelength range is observed (see Figure 4a). This fastening model could represent a situation where (more) degradation, e.g. railpad wear, occurs at the leading and trailing sides of the fastening, changing the constraining condition of the rail and allowing more flexibility in the longitudinal direction. This fastening condition, i.e. RPM3, is now considered a possible effective *initial excitation* and is examined in the next sections.

4.2. Initial differential wear

With this initial excitation RPM3, the spatial and wavelength domain distributions of the differential wear were obtained with the FE model of Section 3 and are shown along with those of RPM1 in Figure 4(a, b). With RPM3, there are four main wavelength components after bandpass filtering in the range of 20–80 mm, namely, 39.4 mm (corresponding to 987 Hz with a traffic speed of 140 km/h), 33.3 mm (1168 Hz), 28.6 mm (1360 Hz) and 24.9 mm (1562 Hz). The wavelength of 28.6 mm has the highest power spectral density (PSD) magnitude and is thus dominant. The differential wear of RPM1 has much lower power intensity magnitudes in the wavelength range of 20–80 mm and is thus unable to initiate corrugation.

Figure 4(c–g) show field observations of corrugation on the Dutch railway network. The spatial distribution of the simulated differential wear of RPM3 in Figure 4(a) has a pattern similar to the field corrugation in Figure 4(c); they both have an amplitude periodicity of approximately 8–9 wavelengths [26]. Such periodicity is clearly visible in the field measurement, as indicated in Figure 4(e), where $2A_{\max} = 32.4 \mu\text{m}$. Although such periodicity is not clearly present in the measurement of Figure 4(f), the main wavelength components of the 2 measurements are the same, i.e. 28.6 mm (Figure 4(d)), and they are in good agreement with those from the simulation with RPM3 (Figure 4(b)). The agreement between the simulation and the field observation is because the model uses parameters of the typical Dutch railway, and the model has been calibrated and validated in previous research for the Dutch situation [26,62,63]. There are 4 components approximately 28.6 mm from the simulation. In each of the measurements, there are multiple wavelength components longer than 28.6 mm. Both the field data and the modelling show that multiple vibration components co-act. The apparent overall wavelength seen in Figure 4(c) is a combination of all the co-acting wavelengths. The difference between the 2 measurements is due to the variability that commonly exists along railway tracks. Figure 4(g) shows a periodicity variation in the field marked by the squats. The most severe squats took place at the largest corrugation amplitude, and the periodicity has 11 and 9 wavelengths in the figure.

4.3. Longitudinal force dominates corrugation initiation

The initial differential wear reflects the dynamic behaviour of the wheel-rail interactions in the vehicle-track system, which determines the initial wavelength of the corrugation. The contact forces, due to the wheel-rail dynamic interaction, act as the input to the damage mechanism, causing wear. The relationship between the initial differential wear and the dynamic contact forces is studied in this section.

Figure 5 shows the differential wear (W_f) and the corresponding longitudinal (F_L) and vertical (F_N) contact forces in the spatial and wavelength domains. In the spatial domain, as shown in Figure 5(a), W_f and F_L are highly correlated, with approximately the same phase and with the same trend of amplitude variation, e.g. the larger amplitudes near 0.575 m and 0.75 m. The slight phase difference between them is inherently because F_L is the sum of the longitudinal shear stress over the entire contact patch, while wear only appears at the rear part of the contact patch where microslip exists [62]. Further PSD analysis in Figure 5(b) confirms that all four main wavelength components of the wear can find their respective counterparts in the PSD of F_L , with a corresponding wavelength and magnitude. The vertical contact force shows almost no correlation with the wear in neither the spatial domain nor the wavelength domain. Therefore, we can conclude that F_L dominates the initial differential wear and thus corrugation initiation.

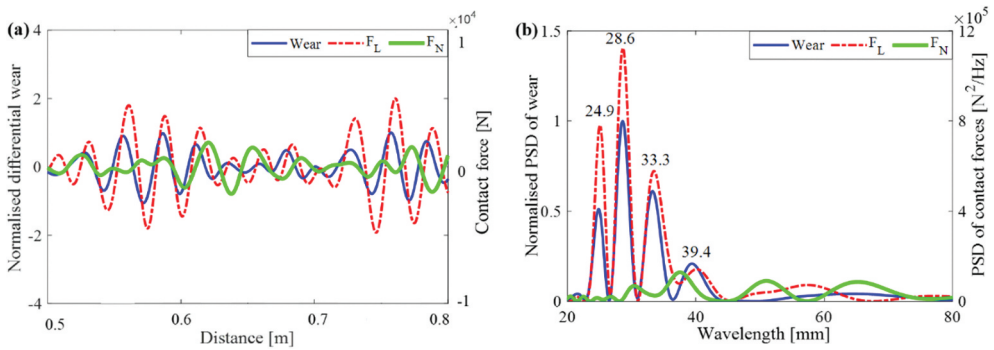


Figure 5. Comparison between the initial differential wear and the contact forces (bandpass filter 20–80 mm) of RPM3 in the spatial and wavelength domains. (a) in the spatial domain (b) in the wavelength domain.

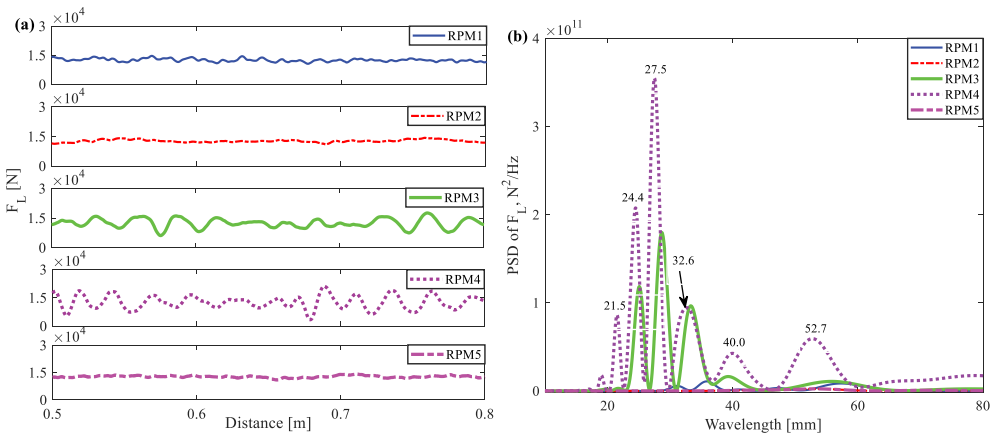


Figure 6. Longitudinal contact forces F_L under RPM1–5. (a) F_L in the spatial domain and (b) F_L in the wavelength domain. The wavelength numbers shown in the plot are for RPM4, and the curve for RPM3 is the same as that in Figure 5b. The results were obtained with $2a_{max} = 0$ (smooth rail).

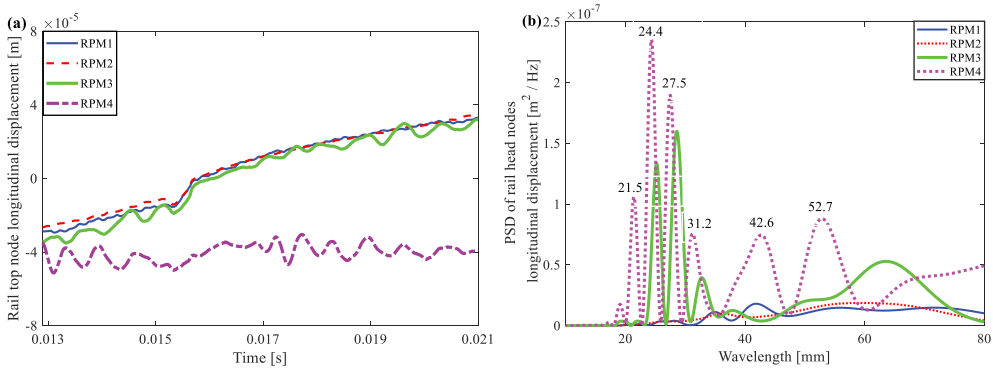


Figure 7. Longitudinal displacement of a node in the middle of the rail top surface at $x = 0.6$ m when the wheel rolls from the left side at $x = 0.5$ m over the node to the right until $x = 0.8$ m (nodes are from a cross-section next to 0.6 m to avoid the influence from the fastening constrained boundary). (a) node displacement in the time domain and (b) node displacement in the wavelength domain. The wavelength numbers shown in the plot are for RPM3 (green) and RPM4 (black). The results were obtained with $2a_{max} = 0$ (smooth rail).

4.4. The corrugation-initiating wear is caused by rail longitudinal compression modes

In this section, we further examine what happens in the rail concerning the wheel-rail contact and show, as proposed in [26] and observed in the preceding section, that it is the rail longitudinal compression modes [76,77], instead of the rail vertical bending or longitudinal shear, that are dominant for corrugation initiation. To this end, RPM1–5 in Table 1 are designed to identify the vibration mode that is responsible for the initial differential wear of the corrugation.

4.4.1. Vertical rail bending is not responsible for corrugation initiation

We first show that the vertical rail bending mode is not responsible for the initial differential wear.

Figure 6 shows F_L under the different fastening conditions RPM1–5. Vertical bending is allowed in RPM3 but not in RPM4. Compared to RPM3, the vertical degrees of freedom of all the nodes at the rail bottom are rigidly constrained in RPM4. From Figure 6a, 6b both RPM4 and RPM3 have large F_L values, indicating that vertical rail bending is not a decisive factor for F_L .

However, RPM1 and RPM2 also allow vertical bending as RPM3, whereas the F_L values of RPM1 and RPM2 have negligible PSD magnitudes compared to those of RPM3 and RPM4 in Figure 6b. This is because, as listed in Table 1, RPM3 and RPM4 are longitudinally constrained only at the middle column, whereas RPM1 and RPM2 are more strongly and rigidly constrained in the longitudinal direction. This indicates that the longitudinal vibrational modes are much more important than the vertical bending for the fluctuation of F_L . Additionally, from Figure 6a, RPM2 exhibits almost no fluctuation, whereas RPM1 still has some fluctuation. Compared to RPM1, whose longitudinal rigid constraint is only applied at the 3 columns of the fastening, RPM2 rigidly constrains all the nodes of the rail foot bottom in the longitudinal direction. This result again indicates the dominance of rail longitudinal vibration in the fluctuation of F_L .

Figure 7 further shows the displacement of a node in the middle of the rail contact surface to analyse the effect of rail vertical bending on corrugation initiation. This node is at position 0.6 m inside the solution zone and is above a sleeper. When rail vertical bending is allowed, as is the case by RPM1–3, the node displacement follows an overall rising trajectory when the wheel rolls over it from left to right (Figure 7a). The PSD of the node displacement (Figure 7b) generally agrees with the PSD of F_L (Figure 6b), except for the relative magnitude of the corresponding wavelength components. When the bending motion of the rail is not allowed as by RPM4, the displacement of the node is generally horizontal, fluctuating around -40 μm , i.e. without the overall rising trend (Figure 7a). Its overall negative value is due to the backward shear deformation caused by the longitudinal tangential force. This analysis confirms that the overall rising longitudinal

displacement in Figure 7a with RPM1–3 is due to the vertical bending of the rail. The exclusion of rail vertical bending vibration in RPM4 suppresses the overall rising longitudinal displacement but cannot prevent the fluctuations of F_L , the longitudinal displacement and the initial differential wear. It is RPM1 and RPM2 that have negligible PSD of the longitudinal nodal displacement because of their stronger longitudinal constraints.

In summary, these observations show that the vertical bending vibration is not responsible for corrugation initiation.

4.4.2. Longitudinal rail shear is not responsible for corrugation initiation

After excluding the vertical bending vibrations, in this section, we investigate whether rail longitudinal sheared vibration and/or longitudinal compression/rarefaction vibration are responsible for corrugation initiation. To this end, RPM4 and RPM5 are designed and compared. With RPM4, the rail foot bottom is continuously and rigidly constrained in the vertical direction, but in the longitudinal direction, only the motion of the central column spring-damper elements is rigidly constrained. With RPM5, the rail foot bottom is constrained continuously and rigidly in both the vertical and longitudinal directions.

Longitudinal contact forces with RPM4 and RPM5 are shown in Figure 6. Only the model with RPM4 can develop corrugation. It can be observed that the responses with RPM5 are rather flat with only minor fluctuations. With such a longitudinal contact force, the initial differential wear would not be sufficient to develop corrugation; then, with RPM5, corrugation would not initiate or grow.

Figure 8(a,b) show the longitudinal displacements of three nodes located in the middle of the rail top surface (Node 1), at the rail web (Node 2), and at the rail foot (Node 3) in the same cross-section using RPM4 and RPM5, respectively. Figure 8(b,d) show the displacements of the cross-section (in magenta) relative to the original rail cross-section without loading (in green) at three moments: before contact, during contact and after contact with the wheel. The rolling direction of the wheel is from left to right in the figure; see the velocity vector v .

In Figure 8(a), with RPM4, the longitudinal displacements of the three nodes are characterized by a constant component superposed with a fluctuation component varying over time. The constant components are approximately -4×10^{-5} m for the rail top, 0 m for the rail web and 2.5×10^{-5} m for the rail foot. The three constant components can be explained by the longitudinal sheared motion, which appears consistently at the three moments in Figure 8(b) (before, during and after contact with the wheel). The rail cross-section at the three moments is sheared in the direction opposite to the wheel rolling direction due to the applied traction, with the rail top moving backward (to the left of the figure) and the rail foot moving forward (to the right of the figure), both relative to the original rail cross-section. Furthermore, the fluctuation components of the longitudinal displacement of the three nodes are synchronous, i.e. in-phase fluctuation and approximately equal in amplitude. This means that the fluctuation component that may cause corrugation corresponds to an in-phase vibration over the whole rail cross-section, which should be the rail longitudinal compression vibration. The results in Figure 8(a,b) indicate that with RPM4, the rail in the longitudinal direction can experience both longitudinal sheared and longitudinal compression/rarefaction vibrations.

In Figure 8(c), with RPM5, the longitudinal displacements of the three nodes are almost constant, i.e. without fluctuation, during the whole simulation due to the continuous and rigid longitudinal constraint. The magnitudes are approximately -6×10^{-5} m for the node at the rail top, -2×10^{-5} m at the rail web, and 0.2×10^{-5} m at the rail foot. The constant component with RPM5 at the rail head and the rail web is longitudinal sheared vibrations opposite to the rolling direction due to traction. The rail foot is rigidly constrained in the longitudinal direction, and the longitudinal displacement is shown as a flat line at 0 m (Figure 8(c,d)). The fluctuation component, which corresponds to longitudinal compression/rarefaction vibrations, as explained in RPM4, does not appear in the longitudinal displacement of the three nodes with RPM5 in Figure 8(c). The results in Figure 8(c,d) suggest that with RPM5, only longitudinal sheared motion of the rail is allowed in the

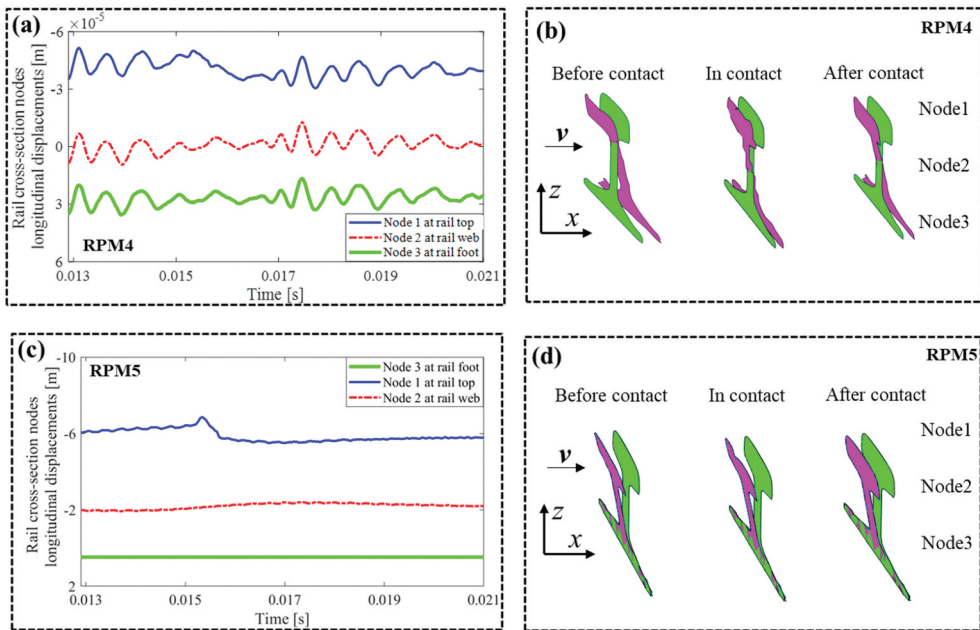


Figure 8. Longitudinal displacement of three nodes (node 1 is in the middle of rail top surface; node 2 in the rail web; node 3 in the rail foot) in a rail cross-section at $x = 0.6$ m when the wheel rolls from the left side at $x = 0.5$ m ($t = 0.0129$ s) to the right side until $x = 0.8$ m ($t = 0.0206$ s) with (a) RPM4 and (c) RPM5. The black downward arrows in (a) and (c) indicate that the 3 curves in each of the 2 plots are in the sequence from the rail top to the rail foot. The displacements of the cross section relative to the original rail cross section without loading in (b) RPM4 and (d) RPM5 (Green: the original rail cross section; Magenta: the rail cross section after deformation.). The results were obtained with $2a_{\max} = 0$ (smooth rail).

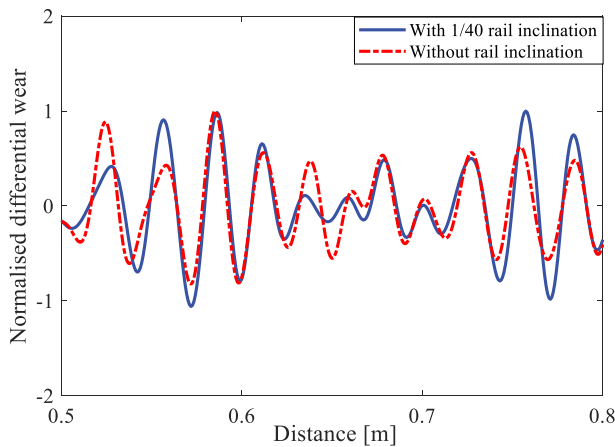


Figure 9. Comparison of the differential wear W_f with and without 1/40 rail inclination under RPM3 (bandpass filter 20–80 mm). The results were obtained with $2A_{\max} = 0$ (smooth rail).

longitudinal direction. The local peak displacement of node 1 between 0.015 and 0.016 s in Figure 8(c) is the rail top displacement due to the wheel-rail contact that passes over node 1.

In conclusion, the rail longitudinal sheared vibration is present in both models RPM4 and RPM5, and longitudinal compression/rarefaction vibration is only present in model RPM4. As RPM4 can develop corrugation while RPM5 cannot, we conclude that longitudinal sheared vibration is not relevant for corrugation formation.

4.4.3. The corrugation-initiating wear is caused by longitudinal rail compression modes

After excluding the vertical rail bending in Section 4.4.1 and the longitudinal rail shear in Section 4.4.2, it is concluded that longitudinal rail compression modes, which are identified as in-phase longitudinal vibration over the whole rail cross-section in Figure 8(a), are decisive for corrugation-initiating wear. With RPM3 and RPM4, the simulation results indicate corrugation can continuously grow at least up to 40 μm with the consistency condition met. In the sections below, we will discuss in detail the necessary consistency conditions for corrugation growth with RPM3. In summary, among the 5 fastening models, RPM1, RPM2 and RPM5 do not allow corrugation occurrence, and RPM3 and RPM4 allow corrugation formation. RPM3 and RPM4 are thus considered as effective initial excitations.

4.4.4. The influence of rail inclination is negligible

With RPM1–5, the rail inclination is 1/40. In the abovementioned analysis, the influence of the inclination is not considered, as with rail inclination, the lateral and torsional rail modes can also be involved in the wheel-rail dynamic interactions. This influence is now evaluated with RPM3 by comparing the differential wear calculated with and without 1/40 inclination. Figure 9 shows the distributions of the initial differential wear in the spatial domain. These distributions have the same wavelength and phase angle. Note that there is a slight difference in the amplitude. However, this difference does not influence the corrugation wavelength and phase angle, which determine the consistent corrugation initiation and growth. Therefore, the consistency in the initiation and growth of corrugation is still valid. It can be concluded that the 1/40 rail inclination has a negligible influence on the initial differential wear and corrugation formation.

5. Consistent growth of corrugation

This section discusses, by following Steps (b), (c) and (d) of the hypothesis of Section 2, the consistent growth of the corrugation initiated by the differential wear, which is calculated and discussed in Section 4. To this end, trial corrugations that are linearly proportional to and in anti-phase with the calculated initial differential wear of Section 4 under RPM3 (the blue line in Figure 5(a)) are applied to the rail to see if the hypothesis holds.

5.1. Consistency between $2A_{\max} = 0$ and 10 μm

An initial trial corrugation of amplitude $2A_{\max} = 10 \mu\text{m}$ is applied to the rail of the FE model; this corresponds to Step (b). In reality, forming a corrugation with a 10 μm amplitude requires many wheel passages, but here, we assume the corrugation will consistently grow and thus simplify this process by scaling the initial differential wear amplitude to a trial amplitude of 10 μm . The discussion below will indicate our assumption is valid and the corrugation can indeed consistently grow up to 80 μm .

The wheel is then let roll over the corrugated rail. The resulting differential wear W_f due to the joint excitation of both the initial excitation and the initial corrugation is calculated, corresponding to Step (c), and compared in Figure 10. The W_f for $2A_{\max} = 0$ is the same in Figure 10 as in Figure 5.

The differential wear of the smooth rail ($2A_{\max} = 0$) and the initially corrugated rail ($2A_{\max} = 10 \mu\text{m}$) are in phase with each other (Figure 10(a)) and have the same 4 main wavelength components (24.9, 28.6, 33.3, 39.4 mm, Figure 10(b)). Thus, the differential wear caused by joint excitation is consistent in both phase and wavelength with the initial differential wear that is caused by the initial excitation alone so that the initial corrugation will grow; i.e. the condition for consistent initiation and growth is satisfied (Step (d)). By this, the hypothesis is verified to hold for corrugation amplitudes up to 10 μm .

Similar to the initial differential wear caused by the initial excitation alone, all four main wavelength components of the wear at $2A_{\max} = 10 \mu\text{m}$ (Figure 10(b)) can find their respective counterparts in the PSD of F_L in Figure 11(d), with corresponding wavelength and magnitude. The

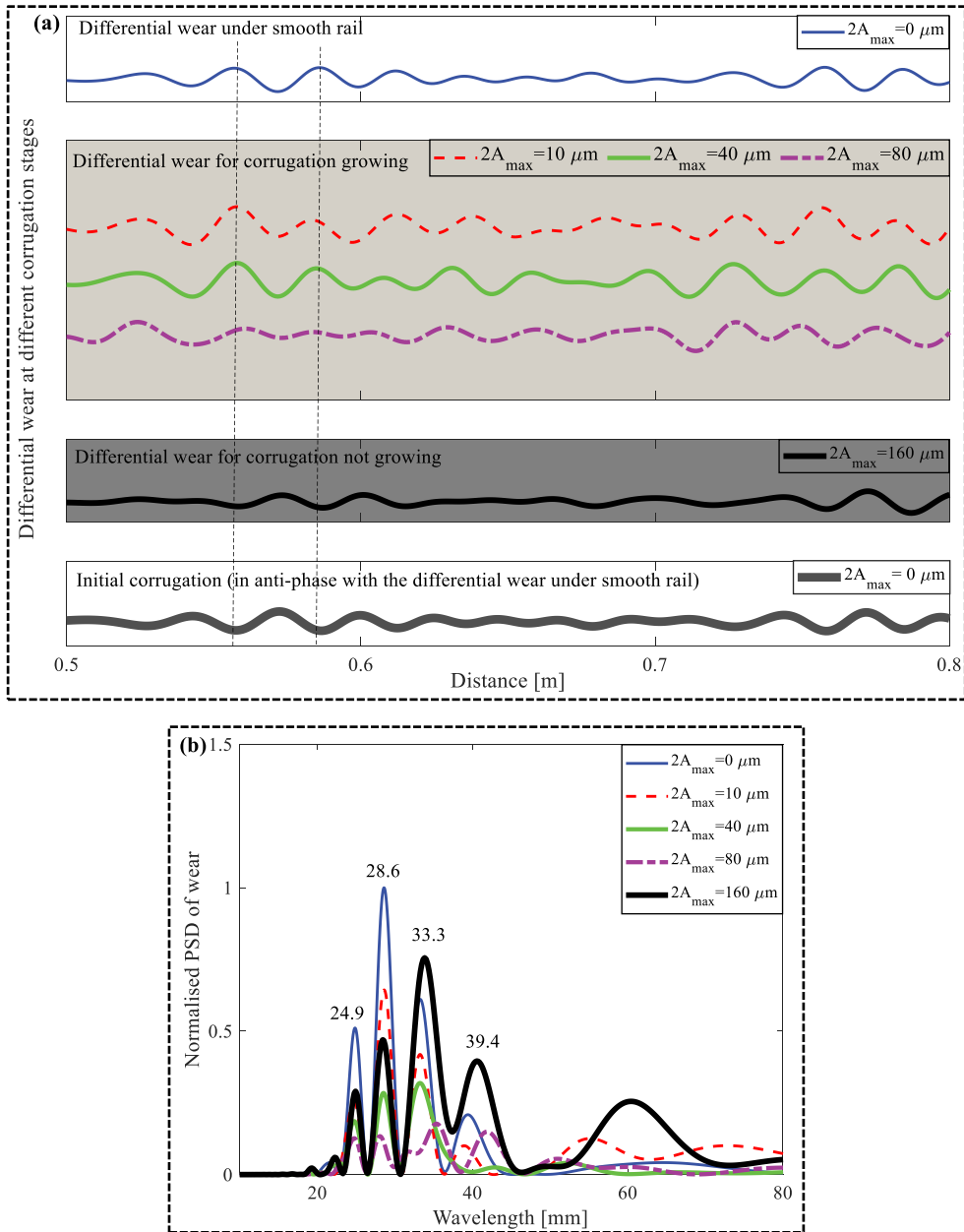


Figure 10. Differential wear W_f with RPM3 with increasing corrugation amplitude. (a) W_f in the spatial domain normalized with the maximum peak-to-trough distance of the initial differential wear. (b) W_f in the wavelength domain normalized with the PSD magnitude of the dominant wavelength component of the wear at $2A_{\max} = 0 \mu\text{m}$. The peak wavelengths at 24.9 mm, 28.6 mm, 33.3 mm and 39.4 mm correspond to $2A_{\max} = 0$.

PSD of the vertical contact force (Figure 11(c)) is small at $2A_{\max} = 10 \mu\text{m}$. Therefore, F_L dominates the initial corrugation growth. And RPM3 is indeed an effective initial excitation that initiates corrugation that consistently grows in the range of 0–10 μm .

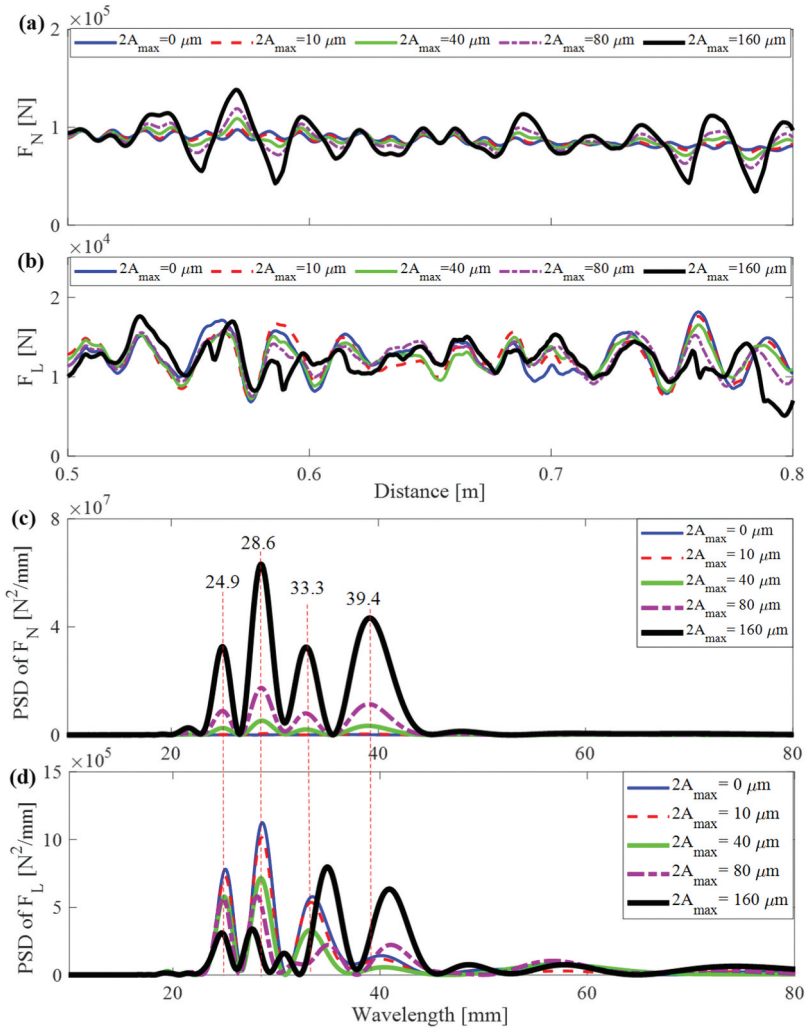


Figure 11. Distributions of the contact forces in the spatial and wavelength domains under RPM3. (a) F_N in the spatial domain; (b) F_L in the spatial domain; (c) F_N in the wavelength domain; and (d) F_L in the wavelength domain.

5.2. Consistency when $2A_{max} > 10 \mu\text{m}$

The next question is as follows: Until what $2A_{max}$ value will corrugation consistently grow? Since the differential wear of the smooth rail and of the initially corrugated rail of $2A_{max} = 10 \mu\text{m}$ are in phase with each other and have the same 4 dominant wavelength components, we further scale the initial corrugation up to larger trial amplitudes $(2A_{max})_i = 40, 80,$ and $160 \mu\text{m}$ to see if the hypothesis still holds. Although the purpose here is to study the consistency with $2A_{max} > 10 \mu\text{m}$, the analysis is carried out in the range of $2A_{max}$ from $0 \mu\text{m}$ to $160 \mu\text{m}$ to obtain an integral picture of the entire corrugation formation process, including both initiation and growth. The calculated differential wear W_f is compared in Figure 10. Figure 11 shows the corresponding vertical and longitudinal contact forces F_N and F_L , respectively, in both the spatial and wavelength domains.

For convenience of quantitative analysis, the wavelength λ and the corresponding passing frequency f are calculated with the traffic velocity v .

$$f = v/\lambda, v = 140\text{km/h} \quad (2)$$

The values are shown in [Table 2](#) for the components of W_f , F_L and F_N presented in [Figures 9 and 10](#), along with those of the trial corrugations. Recall that the amplitude of the trial corrugation is linearly scaled up from the initial W_f , and their wavelength and frequency compositions are identical for all $(2A_{\max})_i = 0, 10, \dots, 160 \mu\text{m}$, $i = 0, 1, 2, \dots$, and are identical to those of the initial W_f .

To link to the eigenfrequencies, the consistency will be checked between the frequencies (f). Nevertheless, wavelengths are first discussed below, as the overall apparent wavelength is what we directly see in real life. The frequencies that correspond to the 6 quantities, i.e. the trial corrugation, W_f , F_L , F_N , f_L and f_N , are

- $f_{2A_{\max}j}$, of the trial corrugation of $2A_{\max}$, with reference frequency components $j = 1, 2, \dots$
- $f_{W_{fij}}$, of W_f , with frequency components $j = 1, 2, \dots$ at $(2A_{\max})_i$, $i = 0, 1, 2, \dots$
- f_{FLij} and f_{FNij} , of F_L and F_N , with frequency components $j = 1, 2, \dots$ at $(2A_{\max})_i$, $i = 0, 1, 2, \dots$
- f_{Lj} and f_{Nj} , of the longitudinal and vertical eigenfrequencies, with frequency components $j = 1, 2, \dots$

The number of main frequency components in each of the 6 quantities is not necessarily the same. There are, for example, only 3 main vertical bending frequencies for RPM3 (see [Table 4 and 9](#)), whereas for most of the other quantities, there are 4 main components. The number of main frequency components is also not necessarily constant for a specific quantity due to, e.g. frequency splitting, as will be seen for F_L in [Table 2](#) and the discussion below. For simplicity, however, we use the same subscript j to denote the frequency components in all 6 quantities, as it will not affect our discussion.

The frequencies $f_{2A_{\max}j}$, $f_{W_{fij}}$, f_{FLij} and f_{FNij} follow (2) in relation to their respective wavelengths. The relationship between f_{Lj} , f_{Nj} and their wavelengths will be discussed in [Section 6](#) as a consequence of the frequency selection mechanism.

The wavelengths $\lambda_{2A_{\max}j}$ and corresponding frequencies $f_{2A_{\max}j}$ of the trial corrugation are chosen as the reference for the consistency analysis because the frequencies $f_{2A_{\max}j}$ are directly linked to the other 5 quantities. That is, it is the same as $f_{W_{f0j}}$ of the initial W_f , which is determined by the longitudinal eigenfrequencies f_L and the associated F_L ; it excites the vertical eigenfrequencies f_N and the associated F_N . Via (2), the frequencies are uniquely related to their respective corresponding wavelengths. Thus, wavelength and frequency are hereunder used interchangeably.

For comparison and trend analysis, relative deviations and relative differences are used. A (relative) deviation is defined as the absolute value of the difference between a wavelength (or frequency) and its reference wavelength $\lambda_{2A_{\max}j}$ (or frequency $f_{2A_{\max}j}$) divided by the reference wavelength (or frequency). For example, in terms of wavelength λ_j ,

$$\text{Deviation} = |\lambda_j - \lambda_{2A_{\max}j}| / \lambda_{2A_{\max}j} \quad (3)$$

A (relative) difference is defined similarly, but not relative to the reference wavelength $\lambda_{2A_{\max}j}$ and frequencies $f_{2A_{\max}j}$. For example, in terms of wavelength λ_j ,

$$\text{Difference} = |\lambda_j - \lambda_{ij}| / \lambda_{ij}, \lambda_{ij} \neq \lambda_{2A_{\max}j} \quad (4)$$

See examples of deviations in [Table 2](#) and examples of differences in [Table 5](#). A quantity with a small deviation or difference clearly has high consistency with its denominator $\lambda_{2A_{\max}j}$ or λ_{ij} .

Among all 6 quantities, the 3 quantities W_f , F_L and F_N change with $(2A_{\max})_i$, $i = 0, 1, 2, \dots$. The consistency of these 3 quantities is first examined by looking at the trend of their deviations with increasing $2A_{\max}$. Then, the roles of f_L and f_N in the consistency development are discussed by looking at the relative deviations and differences in W_f , F_L , F_N and f_L and f_N . This leads to the identification of a frequency selection mechanism that can explain the seemingly wavelength ‘fixing’ of the corrugation, as discussed below.

Table 3. Consistency between the wavelength components of the 3 quantities (W_f , F_L and F_N) with increasing $2A_{\max}$. Case 1 describes the consistency between all 3 quantities. Case 2 describes the consistency between any 2 of the 3 quantities.

Dynamic quantities	Ref λ (mm)	Case 1					Case 2				
		$2A_{\max} = 0$ μm	$2A_{\max} = 10$ μm	$2A_{\max} = 40$ μm	$2A_{\max} = 80$ μm	$2A_{\max} = 160$ μm	$2A_{\max} = 0$ μm	$2A_{\max} = 10$ μm	$2A_{\max} = 40$ μm	$2A_{\max} = 80$ μm	$2A_{\max} = 160$ μm
Trial Corrugation	39,4	0,0%	0,0%	0,0%	0,0%	0,0%	0,0%	0,0%	0,0%	0,0%	0,0%
	33,3	0,0%	0,0%	0,0%	0,0%	0,0%	0,0%	0,0%	0,0%	0,0%	
	28,6	0,0%	0,0%	0,0%	0,0%	0,0%	0,0%	0,0%	0,0%	0,0%	
	24,9	0,0%	0,0%	0,0%	0,0%	0,0%	0,0%	0,0%	0,0%	0,0%	
Differential wear	39,4	0,0%	0,0%	8,6%	6,3%	3,0%	0,0%	0,0%	8,6%	6,3%	3,0%
	33,3	0,0%	0,0%	0,3%	6,0%	1,5%	0,0%	0,0%	0,3%	6,0%	1,5%
	28,6	0,0%	0,0%	0,0%	1,7%	0,3%	0,0%	0,0%	0,0%	1,7%	0,3%
	24,9	0,0%	0,0%	0,0%	0,0%	0,0%	0,0%	0,0%	0,0%	0,0%	0,0%
Longitudinal contact force F_L	39,4	1,0%	1,0%	1,3%	4,1%	3,8%	1,0%	1,0%	1,3%	4,1%	3,8%
	33,3	0,6%	0,3%	0,3%	5,1%	4,8%	0,6%	0,3%	0,3%	5,1%	4,8%
	28,6	0,0%	0,0%	0,3%	1,7%	3,1%	0,0%	0,0%	0,3%	1,7%	3,1%
	24,9	0,4%	0,4%	0,0%	0,4%	0,8%	0,4%	0,4%	0,0%	0,4%	0,8%
Vertical contact force F_N	39,4	4,6%	2,0%	1,0%	0,8%	0,8%	4,6%	2,0%	1,0%	0,8%	0,8%
	33,3	8,7%	0,6%	0,9%	0,9%	0,9%	8,7%	0,6%	0,9%	0,9%	0,9%
	28,6	6,6%	1,4%	0,7%	0,3%	0,3%	6,6%	1,4%	0,7%	0,3%	0,3%
	24,9	1,2%	0,8%	0,0%	0,0%	0,0%	1,2%	0,8%	0,0%	0,0%	0,0%

5.2.1. Relative deviations of W_f , F_L , F_N and the longitudinal and vertical eigenfrequencies

The relative deviations of the wavelengths are calculated and shown in parentheses (next to the wavelengths) in Tables 4 and 5. The reference wavelengths are in boldface. For example, the wavelength component 42.8 mm of the differential wear W_f at $2A_{\max} = 40 \mu\text{m}$ corresponds to the reference wavelength 39.4 mm. Thus, its relative deviation is 8.6%.

Relative deviations are calculated similarly for the eigenfrequencies of the longitudinal compression f_L and vertical bending f_N modes in Table 2, in which the reference values are indicated with ‘w. r.t.’, where necessary.

The wavelength consistency is shown in Table 3 with different colour contrasts: grey, dark green, and light green. In general, light green is related to small deviations and thus strong consistency; dark green is related to intermediate relative deviations and thus weaker consistency; and grey is related to large relative deviation and thus inconsistency. The colour is determined for $2A_{\max} > 0$ by simultaneously satisfying the following three conditions: (i) a number is set to light or dark green if the relative deviations of all 3 (Case 1) or any 2 (Case 2) of the corresponding components are not larger than 3.0%; (ii) with condition (i) being satisfied, a number is set to dark green if its relative deviation is larger than 1.0%; otherwise, it is light green. (iii) Otherwise, a number is set to grey. Taking $2A_{\max} = 40 \mu\text{m}$ as an example, the wavelength components corresponding to a reference wavelength of 39.4 mm are 42.8, 39.9, and 39.0 mm for the differential wear, longitudinal and vertical forces, respectively. They are in grey in Case 1 for all 3 quantities because one of them has a deviation of 8.6%, whereas in Case 2, their colour is grey, dark green and light green because the respective deviations are 8.6%, 1.3% and 1.0%.

Table 4. Comparison of frequency deviations (in brackets) of F_L at $2A_{\max} = 0 \mu\text{m}$ (f_{FL0j}) and longitudinal compression modes f_{Lj} w.r. t. reference frequencies $f_{2A_{\max}j}$.

Reference frequency $f_{2A_{\max}j}$ ($= f_{Wf0j}$)	987	1168	1360	1562
Longitudinal contact force f_{FL0j} (& deviation)	977 (1.0%)	1161 (0.6%)	1360 (0.0%)	1556 (0.4%)
Longitudinal compression mode f_{Lj} (& deviation)	1025 (3.9%)	1187 (1.6%)	1360 (0.0%)	1546 (1.0%)

5.2.2. Development and consistency trend of W_f with increasing $2A_{max}$

First, the behaviour of the wear is examined.

5.2.2.1. The overall consistency of W_f is maintained until $2A_{max} = 80 \mu\text{m}$. Figure 10(a) shows the differential wear W_f with increasing corrugation amplitude in the spatial domain. When $2A_{max}$ is up to $80 \mu\text{m}$, the differential wear is mostly in phase with the initial differential wear and in anti-phase with the initial corrugation, with decreasing amplitudes. When $2A_{max}$ is $160 \mu\text{m}$, the differential wear is mostly in anti-phase with the initial differential wear. These results indicate that the consistent growth trend of W_f breaks at $2A_{max} = 80 \mu\text{m}$. Thus, Step (d) generally holds for $2A_{max}$ up to $80 \mu\text{m}$.

Note that in Figure 10(a), the consistency is seen from the overall wavelength of the wear, which is a combination of all the wavelength components shown in Figure 10(b). In the section below, we show that this overall wavelength development trend is supported by the development trend of the wavelength components. Figure 10(b) shows four groups of wavelength components around the 4 respective reference wavelengths. Each group consists of 5 peaks corresponding to the 5 wavelength components at the 5 values of $2A_{max} = 0, 10, 40, 80$ and $160 \mu\text{m}$. The following observations can be made from Figure 10(b) for the development trend.

5.2.2.2. Wavelength and phase consistency of W_f components breaks at $2A_{max} = 80 \mu\text{m}$. The corrugation amplitude $2A_{max} = 80 \mu\text{m}$ is a breaking point for a consistent wavelength, and the phase development of W_f can be seen from the following observation: (a) When $2A_{max}$ is increased from 0 to $40 \mu\text{m}$, the wavelengths are consistent in all 4 wavelength groups because they stay around their respective initial (i.e. reference) values for all but one of the components. That one exception is the 42.8 mm wavelength component at $2A_{max} = 40 \mu\text{m}$; it has a large relative deviation of 8.6% from the initial value 39.4 mm (see Table 2). However, this component has a negligible PSD compared to the other 3 wavelength components at the same $2A_{max}$ (see Figure 10(b)). Therefore, it has a minor influence on the differential wear and can barely break the consistency of the overall corrugation growth. (b) At $2A_{max} = 80 \mu\text{m}$, the wavelength components at approximately 35.3 and 41.9 mm deviate considerably (6.0% and 6.3%, respectively) from the initial wavelengths of 33.3 and 39.4 mm . They also contain larger PSD magnitudes than those of the other 2 components (see Figure 10(b) and Tables 4 and 5); thus, they are different and strong enough to break the trend of consistent wear growth due to the large change in the wavelength. (c) At $2A_{max} = 160 \mu\text{m}$, although all 4 wavelengths are again close to the initial values, the overall differential wear is in phase and thus inconsistent with the corrugation (see Figure 10(a)). All 4 wavelengths being close to the initial values should be because corrugation with an amplitude of $2A_{max} = 160 \mu\text{m}$ is an excitation that is strong enough to force the differential wear to follow its wavelengths, which are the initial wavelengths by the definition of trial corrugation.

To summarize, the wavelength deviations of the W_f components are in general the largest at $2A_{max} = 80 \mu\text{m}$, and the wear changes between $2A_{max} = 80$ and $160 \mu\text{m}$ from anti-phase with corrugation to in-phase. $2A_{max} = 80 \mu\text{m}$ is thus the breaking point of the consistency of both wavelength and phase development.

5.2.2.3. PSD development trend of the W_f components breaks at approximately $2A_{max} = 80 \mu\text{m}$.

Correspondingly, $2A_{max} = 80 \mu\text{m}$ is also the breaking point of the PSD magnitude decrease trend of wear (Figure 10(b)); with increasing $2A_{max}$, the PSD first decreases, reaching its lowest value at $2A_{max} = 80 \mu\text{m}$, and then increases. This indicates that high consistency in both the wavelength and phase of the differential wear will cause a high wear rate that results in fast corrugation growth.

As contact forces are the direct cause of the wear, the behaviour of the longitudinal and vertical contact forces F_L and F_N are examined in the next section in relation to wear behaviour.

5.2.3. Consistency among W_f , F_L and F_N

The colour contrasts in Table 3 show, with increasing $2A_{\max}$, the wavelength consistency development among the 3 quantities W_f , F_L and F_N . Light green colour means zero or small relative deviations, and thus high consistency; grey is the opposite.

5.2.3.1. F_L wavelength splitting at $2A_{\max} = 80 \mu\text{m}$ sharply increases the wavelength deviations of W_f and F_L but not of

F_N . From Tables 4–5, the deviations and thus the consistency change with increasing $2A_{\max}$. The main change takes place at $2A_{\max} = 80 \mu\text{m}$, where a splitting of the wavelength of the longitudinal contact force F_L occurs; specifically, the component corresponding to reference wavelength 33.3 mm splits into 2, i.e. 31.9 and 35.0 mm, resulting in large relative deviations of 4.2% and 5.1%, respectively. The sharp increase in the deviations happens only to W_f , F_L , but not to F_N , which means that the longitudinal dynamics have no noticeable direct influence on the vertical dynamics. The longitudinal dynamics can indirectly influence the vertical dynamics by causing corrugation and thus vertical excitation.

It is not rare for new vibration frequencies (here, in relation to wavelength/frequency splitting) to appear during the evolution of nonlinear dynamic systems [47,78]. Ewins [78] studied the forced vibration of a bladed disc and reported that the frequency splitting phenomenon is caused by the coupling of a pair of vibration modes with close eigenfrequencies and similar characteristics. Shen *et al.* [47] simulated the wheel-rail impact vibrations at squats and found that new characteristic frequencies can be excited with the evolution of squat geometry, i.e. different lengths and depths. In our case, the wavelength/frequency splitting may be caused by the coupling of the rail longitudinal compression modes whose eigenfrequencies (1025, 1187, 1360 and 1546 Hz in Tables 4 and 6) are close to the reference frequencies, and they are excited by the increased corrugation amplitudes, i.e. $2A_{\max} = 80 \mu\text{m}$. This wavelength splitting coincides with the breaking of wear growth trends at $2A_{\max} = 80 \mu\text{m}$ discussed above.

Corresponding to this splitting of wavelengths, the number of inconsistent wavelengths of the 3 quantities at $2A_{\max} = 80 \mu\text{m}$ grows sharply to 7 (in grey, case 1 in Table 3), with another 2 wavelengths turned into dark green, much more than the number of consistent wavelengths (4, in light green). In contrast, the only 3 inconsistent wavelengths at $2A_{\max} = 40 \mu\text{m}$, i.e. before splitting, correspond to the longest reference wavelength of 39.4 mm. Recall that the PSD of W_f at 39.4 mm is the weakest and thus least influential among the 4 reference wavelengths at $2A_{\max} = 40 \mu\text{m}$; see Figure 10b and the discussion above.

5.2.3.2. The wavelength consistency of F_L and F_N decreases and increases, respectively, continuously with increasing

$2A_{\max}$. From Case 2 of Table 3, two trends can be observed with increasing $2A_{\max}$: (1) the consistency of the longitudinal force with either of the other 2 quantities continuously decreases. This agrees with the observation from Case 1 that the consistency between the 3 quantities decreases with increasing $2A_{\max}$. This is because of the pushing and disturbing effects to be discussed below in relation to resonance at eigenfrequencies. (2) The consistency between the vertical force and the wear continuously increases because of the increasing excitation of the corrugation that is proportional to the initial differential wear and that causes the vertical dynamic wheel-rail interaction force.

5.2.3.3. The wavelength consistency of W_f with F_L and F_N is the lowest at $2A_{\max} = 80 \mu\text{m}$. As a result of the interplay between these 2 trends, the wavelength consistency of W_f with F_L and F_N in Case 2 (in terms of the number of light green numbers) first decreases until $2A_{\max} = 80 \mu\text{m}$ to the lowest (i.e. with only 1 wavelength (24.9 mm) in light green) and then increases. This occurs with the decreasing consistency of W_f with and thus decreasing dominance of the longitudinal vibration, as well as with the increasing dominance of the vertical vibration (but then the phase of the wear

becomes inconsistent). This is the cause of the above observation that the wavelength deviations of the wear are the largest at $2A_{\max} = 80 \mu\text{m}$, with the corresponding PSD being the lowest, and the wear changes approximately $2A_{\max} = 80 \mu\text{m}$ from being anti-phase with corrugation to being in-phase.

5.2.3.4. Increasing $2A_{\max}$ favours the growth of longer wavelength components. Referring to Figure 11, the amplitude fluctuation of F_N and its PSD increase monotonously with increasing corrugation amplitude (Figure 11(a,c)), as the vertical force is a response to the excitation by corrugation. The PSD of F_N is negligibly small for $2A_{\max} < 40 \mu\text{m}$.

On the other hand, the amplitude of the F_L (Figure 11(b)) shows no such trend but varies depending on the position along the track, indicating a weaker correlation between the longitudinal force and the corrugation excitation. The PSD of F_L (Figure 11(d)) shows, with increasing $2A_{\max}$, a decreasing dominance of the longitudinal vibration until $2A_{\max} = 80 \mu\text{m}$. After that, it shows 2 different trends: (a) for the 2 groups of shorter wavelengths of approximately 24.9 and 28.6 mm, their F_L PSD continues to monotonously reduce with increasing $2A_{\max}$. (b) For the 2 groups of longer wavelengths of approximately 33.3 and 39.4 mm, the F_L PSD first decreases with increasing $2A_{\max}$ until approximately $2A_{\max} = 80 \mu\text{m}$ and then increases. The reason for these different trends is because a larger $2A_{\max}$ tends to require a longer time per cycle in the vertical wheel-rail interaction. A longer interaction time excites lower frequency vibrations in both the vertical and longitudinal directions, causing more longer wavelength wear, hence favouring longer wavelength growth.

5.2.3.5. F_L wavelength splitting and its longer wavelength components break the growth trend of W_f at $2A_{\max} = 80 \mu\text{m}$. Compared with $2A_{\max} \leq 40 \mu\text{m}$, in Figure 11(d), there are two new and weak wavelength components in F_L due to wavelength splitting: 31.9 mm at $2A_{\max} = 80 \mu\text{m}$ and 30.7 mm at $2A_{\max} = 160 \mu\text{m}$. The other wavelength components of the splitting (35.0 mm at $2A_{\max} = 80 \mu\text{m}$ and 34.9 mm at $2A_{\max} = 160 \mu\text{m}$) are stronger (higher PSD in Figure 11(d)) and longer. The stronger and longer ones can clearly find their counterparts in the differential wear in Figure 10(b) (see also Table 2): The 35.0 mm at $2A_{\max} = 80 \mu\text{m}$ and 34.9 mm at $2A_{\max} = 160 \mu\text{m}$ of the longitudinal force F_L correspond to the 35.3 mm and 33.8 mm components in the wear. The weak and shorter splitting F_L component of 31.9 mm for $2A_{\max} = 80 \mu\text{m}$ can find a corresponding weak peak at approximately 31 mm in the PSD of the wear (Figure 10(b)). No counterpart can be found in the wear (Figure 10(b)) for the weak 30.7 mm component of F_L at $2A_{\max} = 160 \mu\text{m}$, probably due to its large deviation (7.3%) and the strong dominance of the vertical excitation. This new 30.7 mm F_L component looks in Figure 11(d) like a ‘separator’ between the 2 groups of shorter wavelengths and the 2 groups of longer wavelengths.

The 2 groups of longer wavelength components thus become, due to the splitting, even longer. Since increasing $2A_{\max}$ favours the growth of longer wavelength components, the increased corrugation amplitude $2A_{\max} = 80 \mu\text{m}$, the resulting F_L wavelength splitting and the increased wavelengths of the longer wavelength components cause the breaking of the wear growth trend.

As seen from the above analysis, W_f has 4 main components, the development of which are closely related to the 4 components of F_L and F_N . Links are observed between them and the eigenfrequencies of the system, as well as their excitation and splitting. There are 4 longitudinal compression modes in the frequency range of the W_f , F_L and F_N components (Table 2). There are, however, only 3 vertical bending modes in the same range. Since eigenfrequencies are inherent and fundamental characteristics of dynamic systems, links between corrugation and eigenfrequencies are sought below.

5.3. Consistency with eigenfrequencies

The frequencies of the longitudinal compression f_L and vertical bending modes f_N close to the frequencies of the differential wear f_{Wf} and longitudinal and vertical forces f_{FL} and f_{FN} are shown in Table 2 for RPM3.

5.3.1. Good consistency among Wf , F_L and the longitudinal modes at $2A_{max} = 0 \mu m$

A comparison between the frequencies of the initial differential wear f_{Wf0j} (i.e. the reference frequencies $f_{2A_{max}j}$), the F_L at $2A_{max} = 0 \mu m$ (f_{FL0j}), and the longitudinal compression modes f_{Lj} is shown in Table 4. There is a good correspondence between the relative deviations of f_{Lj} and f_{FL0j} ; e.g. a large deviation from the eigen vibration mode corresponds to a large deviation of the force. Furthermore, the mode with the largest deviation has the lowest PSD in Figure 10(b) (the 39.4 mm wavelength, corresponding to 1025 Hz), and the mode with the smallest (actually null) deviation has the highest PSD (the 28.6 mm wavelength, corresponding to 1360 Hz). This indicates a strong correlation and consistency between the longitudinal compression modes f_L , the longitudinal contact force f_{FL0j} and the resulting differential wear f_{Wf0j} at $2A_{max} = 0 \mu m$. It shows that better frequency consistency between them causes a higher wear rate, in line with the observation made above that the consistent wavelength and phase of differential wear causes a high wear rate that results in fast corrugation growth.

This can enable a consistent initiation and initial growth process. That is, the initial excitation excites the longitudinal compression modes, causing the 4 resonant longitudinal contact force components around the 4 eigenfrequencies, producing the consequent differential wear and corrugation. With $v = 140$ km/h, 1360 Hz is the exact resonance frequency of the 28.6 mm wavelength F_L , so that a 100% consistency in wavelength and phase exists among the components of the longitudinal force, differential wear and corrugation of this frequency until $2A_{max} = 10 \mu m$; its differential wear has zero deviation and is the strongest until $2A_{max} = 40 \mu m$ (Figure 10(b)). This is in good agreement with the field observations of Figure 4(d–f), which show a dominant wavelength at 28.6 mm, with $2A_{max} = 32.4 \mu m$ in Figure 4(e).

5.3.2. Decreasing consistency between F_L and the longitudinal modes with increasing $2A_{max}$

The consistency between F_L and the longitudinal compression modes decreases with increasing $2A_{max}$, as seen from the increasing relative difference in Table 5a. This is caused by the increasing disturbing effect of the vertical excitation and wavelength splitting. The disturbing effect will be discussed below. This decrease in consistency is a cause of the decreasing dominance of the longitudinal vibration with increasing $2A_{max}$.

5.3.3. Consistency between Wf and the longitudinal modes is highest at $2A_{max} = 0 \mu m$

Table 5b shows that the consistency between W_f and the longitudinal modes is highest at $2A_{max} = 0 \mu m$. The deviations do not monotonously decrease with increasing $2A_{max}$ because the largest inconsistency does not take place at $2A_{max} = 160 \mu m$ but at approximately $2A_{max} = 80 \mu m$, where splitting takes place.

Table 5a. Frequency difference in F_L w.r.t. the longitudinal compression modes.

Longitudinal compression mode f_{Lj} (Hz)	$2A_{max}$ (μm)	1025	1187	1360	1546
Longitudinal contact force	0	977 (4.7%)	1161 (2.2%)	1360 (0.0%)	1556 (0.6%)
f_{FLij} (Hz) (& difference)	10	977 (4.7%)	1165 (1.9%)	1360 (0.0%)	1556 (0.6%)
	40	975 (4.9%)	1172 (1.3%)	1365 (0.4%)	1562 (1.0%)
	80	949 (7.4%)	1111 (6.4%)	1384 (1.8%)	1569 (1.5%)
			1219 (2.7%)		
	160	951 (7.2%)	1115 (6.1%)	1404 (3.2%)	1575 (1.9%)
			1267 (6.7%)		

Table 5b. Frequency difference in W_f w.r.t. the longitudinal compression modes.

Longitudinal compression mode f_{Lj} (Hz)	$2A_{max}$ (μm)	1025	1187	1360	1546
Differential wear f_{Wfj} (Hz) (& difference)	0	987 (3.7%)	1168 (1.6%)	1360 (0.0%)	1562 (1.0%)
	10	987 (3.7%)	1168 (1.6%)	1360 (0.0%)	1562 (1.0%)
	40	909 (11%)	1172 (1.3%)	1360 (0.0%)	1562 (1.0%)
	80	929 (9.4%)	1102 (7.2%)	1386 (1.9%)	1562 (1.0%)
	160	959 (6.4%)	1151 (3.0%)	1367 (0.5%)	1562 (1.0%)

Table 6. Comparison of the frequencies (Hz) and deviations of W_f and F_N at $2A_{max} = 0 \mu\text{m}$ (f_{Wf0j} , f_{FN0j}), as well as vertical bending modes f_{Nj} .

Reference frequency f_{2Amaxj} ($= f_{Wf0j}$)	987	1168	1360	1562
Vertical contact force f_{FN0j} (& deviation)	1035 (4.6%)	1280 (8.7%)	1457 (6.6%)	1581 (1.2%)
Vertical bending mode f_{Nj} (& deviation)	987 (0.0%)	1117 (4.4%)	Missing	1553 (0.6%)

The largest W_f difference at 1025 Hz (11%) in Table 5b occurs at $2A_{max} = 40 \mu\text{m}$, instead of $80 \mu\text{m}$. The PSD of W_f at $2A_{max} = 40 \mu\text{m}$ is, however, negligible (see Figure 10(b)). This large difference thus does not affect the overall consistency.

5.3.4. Poor correlation between F_N and the vertical modes at $2A_{max} = 0 \mu\text{m}$

A comparison among the frequencies of the initial differential wear f_{Wf0j} ($= f_{2Amaxj}$), the initial F_N and the vertical bending modes (f_{FN0j} , f_{Nj}) is shown in Table 6. Three groups of vertical bending modes are found for the 3 reference frequencies of 987, 1168 and 1562 Hz, with the respective closest vertical eigenfrequencies (and the relative deviations) being 987 (0.0%), 1117 (4.4%) and 1553 (0.6%) Hz. They correspond to the 3 vertical force components of 1035, 1280, and 1581 Hz at $2A_{max} = 0 \mu\text{m}$, the relative deviations of which are 4.6%, 8.7% and 1.2%, respectively. No nearby eigenfrequency was found for the reference frequency of 1360 Hz.

The correlation between the relative deviations of the eigenmodes f_{Nj} and of the force components F_{N0j} is poor, if any. The vertical mode at 987 Hz has zero deviation relative to the reference frequency of 987 Hz, but this 987 Hz is not relevant to the 987 Hz of the differential wear, as shown in Section 4.4.1.

5.3.5. Consistency among W_f , F_N and the vertical modes is the lowest at $2A_{max} = 0 \mu\text{m}$

Table 7 shows that the consistency among the W_f , F_N and the vertical modes is the lowest at $2A_{max} = 0 \mu\text{m}$. The consistency between F_N and the vertical modes largely monotonously increases with increasing $2A_{max}$, as shown in Table 7a. The difference in W_f w.r.t. the vertical modes change the most at approximately $2A_{max} = 80 \mu\text{m}$ (see Table 7b). Note that the relative differences are shown in their absolute values. The difference is actually -1.3% for the 1102 Hz W_f at $2A_{max} = 80 \mu\text{m}$. The change is therefore larger than that seen in Table 7b.

Hence, a correlation and a consistency are lacking between the frequencies of the vertical modes and the vertical contact force at $2A_{max} = 0 \mu\text{m}$. In other words, the initial differential wear and

Table 7a. Frequency difference in F_N w.r.t. the vertical bending modes.

Vertical bending mode f_{Nj} (Hz)	$2A_{max}$ (μm)	987	1117	Missing	1553
Reference frequencies f_{2Amaxj} (Hz) (& deviation)		987 (0.0%)	1168 (4.4%)	1360 (100%)	1562 (0.6%)
Vertical contact force f_{FNj} (Hz) (& difference)	0	1035 (4.9%)	1280 (15%)	–	1581 (1.8%)
	10	1008 (2.1%)	1175 (5.2%)	–	1550 (0.2%)
	40	997 (1.0%)	1179 (5.6%)	–	1562 (0.6%)
	80	995 (0.8%)	1179 (5.6%)	–	1562 (0.6%)
	160	995 (0.8%)	1179 (5.6%)	–	1562 (0.6%)

Table 7b. Frequency difference in W_f w.r.t. the vertical bending modes.

Vertical bending mode f_{Nj} (Hz)	$2A_{\max}$ (μm)	987	1117	Missing	1553
Differential wear f_{Wfj} (Hz) (& difference)	0	987 (0.0%)	1168 (4.6%)	–	1562 (0.6%)
	10	987 (0.0%)	1168 (4.6%)	–	1562 (0.6%)
	40	909 (7.9%)	1172 (4.9%)	–	1562 (0.6%)
	80	929 (5.9%)	1102 (1.3%)	–	1562 (0.6%)
	160	959 (2.8%)	1151 (3.0%)	–	1562 (0.6%)

corrugation cannot be linked to the vertical bending modes. Indeed, in [Figure 10\(b–d\)](#) for $2A_{\max} = 0$ and $10 \mu\text{m}$, the PSD of F_N is the lowest, whereas the PSD of F_L and the wear are among the highest. The 1360 Hz frequency has the highest PSD, whereas a vertical bending mode is missing around this frequency. Although there is a 100% coincidence between the corrugation frequency and a vertical bending mode at 987 Hz, this vertical mode of 987 Hz is not relevant to the differential wear at 987 Hz. All these are strong evidence of the irrelevance of the vertical bending modes to corrugation initiation. The poor consistency among W_f , F_L and F_N at $2A_{\max} = 0 \mu\text{m}$ is clearly seen by the grey colour in [Table 3](#).

5.4. Consistency between longitudinal and vertical modes determines corrugation formation

It is shown above that with the initial excitation of RPM3, corrugation initiates due to longitudinal rail compression modes; the influences of rail vertical bending, longitudinal shear and inclination are negligible. Once corrugation is initiated, the system is excited by both the initial excitation and corrugation. The excitation of the corrugation increases with the growth of the corrugation amplitude $2A_{\max}$. The highest consistency among W_f , F_L and the longitudinal modes is at $2A_{\max} = 0 \mu\text{m}$, where the consistency between W_f , F_N and the vertical modes is the lowest. With increasing $2A_{\max}$, the consistency of W_f with the longitudinal modes decreases and that with the vertical modes increases. It is, therefore, the consistency between the eigenfrequencies of the longitudinal compression and vertical bending modes that determines the possibility and limiting amplitude $(2A_{\max})_l$ of consistent initiation and growth. $(2A_{\max})_l = 0$ indicates a null chance for consistent initiation and growth. A large $(2A_{\max})_l$ indicates a high degree of consistent initiation and growth. If the eigenfrequencies of the vertical modes coincide 100% with those of the longitudinal modes, would $(2A_{\max})_l$ be infinite? The discussion on how the eigenmodes determine corrugation formation is continued in the next section.

6. Discussion – roles of eigenmodes and mechanism of frequency selection

6.1. Longitudinal resonance determines the central frequency

At $2A_{\max} = 0 \mu\text{m}$, the initial excitation RPM3 determines the 4 main relevant longitudinal eigenfrequencies $f_{Lj} = 1025, 1187, 1360$ and 1546 Hz, as shown in [Table 2](#). When trains pass over RPM3 at $v = 140$ km/h, they are excited, resulting in 4 corresponding F_L components of wavelengths 39.8, 33.5, 28.6 and 25.0 mm, leading to 4 differential wear components with wavelengths 39.4, 33.3, 28.6 and 24.9 mm, respectively. The value of 1360 Hz is the exact passing frequency of 28.6 mm, so that exact resonance occurs. The wavelengths of the corresponding F_L and wear components are equal (both are 28.6 mm); the phase difference between these F_L and W_f components, if any, will remain constant. The frequencies and relative phases of this eigenmode and the corresponding components of F_L and W_f are thus 100% consistent. Consequently, this wear component has the highest PSD; i.e. this wavelength is dominant (see [Figure 10\(b\)](#)). We call this wavelength and the corresponding

Table 8. F_L wavelength deviations vs. F_L wavelength difference w.r.t. longitudinal central wavelength at $2A_{\max} = 0 \mu\text{m}$.

F_L wavelength λ_{FLOj} (mm)	39.8	33.5	28.6	25.0
F_L wavelength deviation w.r.t. the reference wavelength, from Table 2	1.0%	0.6%	0.0%	0.4%
F_L wavelength difference w.r.t. the central wavelength 28.6 mm	39%	17%	0.0%	13%
Longitudinal compression mode f_L (Hz) (& deviation)	1025 (3.9%)	1187 (1.6%)	1360 (0.0%)	1546 (1.0%)

Table 9. Deviations and differences in vertical and longitudinal eigenfrequencies w.r.t. the reference and longitudinal central frequencies.

Reference frequency $f_{2A_{\max}j}$ (Hz)	987	1168	1360	1562
Longitudinal eigenfrequency f_{Lj} (Hz) (& deviation)	1025 (3.9%)	1187 (1.6%)	1360 (0.0%)	1546 (1.0%)
Longitudinal eigenfrequency difference w.r.t. longitudinal central frequency	25%	13%	0.0%	14%
Vertical eigenfrequency f_{Nj} (Hz) (& deviation)	987 (0.0%)	1117 (4.4%)	Missing	1553 (0.6%)
Vertical eigenfrequency difference w.r.t. the longitudinal central frequency	27%	18%	Missing	14%

frequencies, as well as the W_f and F_L components, the longitudinal central wavelength and frequency of the corrugation.

6.2. F_L components are pushed away from their eigenfrequencies by the longitudinal central frequency

Away from the central wavelength, the wavelengths of the F_L components differ from the wavelengths of the W_f components. The farther away from the central wavelength, the larger the differences. Relative to 28.6 mm, the differences in the F_L component wavelengths of 25.0, 33.5 and 39.8 mm are 13%, 17% and 39% for $2A_{\max} = 0 \mu\text{m}$; these differences are roughly proportional to the relative deviations of 0.4%, 0.6 and 1.0%, respectively (see Table 8). Thus, it seems that the relative deviations are caused by the differences in the wavelengths (or frequency) relative to the dominant central wavelength (frequency). In other words, the 3 noncentral F_L wavelengths (frequencies) are ‘pushed’ away from their respective exact resonance wavelengths (frequencies) by the dominant wavelength (frequencies), and the farther away they are from the central wavelength, the more they are being pushed away. Consequently, the consistency decreases when the frequency deviates away from the longitudinal central frequency, with a lower PSD of the wear.

These are true, not only for $2A_{\max} = 0 \mu\text{m}$ but also for all the $2A_{\max}$ values (see Table 5a). With increasing $2A_{\max}$, the noncentral F_L frequencies are pushed and disturbed further away from their corresponding longitudinal eigenfrequencies, although the central F_L frequency also gradually deviates from its corresponding central eigenfrequency, probably in relation to the disturbing effect of the increasing vertical excitation, the inconsistency between the longitudinal and vertical modes, especially the absence of a vertical mode at the central frequency (1360 Hz) and the wavelength splitting.

An exception can be seen in Table 5a; that is, when $2A_{\max}$ increases from $0 \mu\text{m}$ to $40 \mu\text{m}$, the difference in the F_L frequency relative to the 1187 Hz eigenfrequency decreases, instead of increasing due to pushing, by its absolute value from 2.2% (1161 Hz) to 1.3% (1172 Hz). This decreasing trend is ended by the splitting of $f_{FL} = 1172$ at $2A_{\max} = 40 \mu\text{m}$ into 2 frequencies, 1111 and 1219 Hz, at $2A_{\max} = 80 \mu\text{m}$. These frequencies are 1115 and 1267 Hz at $2A_{\max} = 160 \mu\text{m}$. Of the 2 splitting frequencies, 1111 and 1219 Hz, one is below and the other is above both the reference (excitation) frequency 1168 Hz and the corresponding longitudinal eigenfrequency 1187 Hz.

The splitting sharply increases the deviations and differences in the W_f and F_L components in Tables 2 and 5. However, the lower frequency (and thus longer wavelength) one, i.e. 1111 Hz at $2A_{\max} = 80 \mu\text{m}$ and 1115 Hz at $2A_{\max} = 160 \mu\text{m}$, is very close to the vertical eigenfrequency of 1117

Hz. In addition, it approaches 1117 Hz with increasing $2A_{\max}$, probably due to the converging effect to be discussed below.

Both the exception and the splitting happen only to the 1187 Hz eigenfrequency. This seems to suggest a link between the exception and the splitting. As splitting plays an important role in the growth of corrugation, it might be worth further investigating the link in future research.

6.3. Increasing $2A_{\max}$ disturbs F_L away from and converges F_N towards their eigenfrequencies

When corrugation is initiated, the system is excited by both the initial excitation and corrugation of amplitude $2A_{\max} > 0$. Three sets of frequencies are involved: the reference frequencies $f_{2A_{\max j}}$ and the longitudinal and vertical eigenfrequencies f_{Lj} and f_{Nj} , as shown in Table 9. Their corresponding frequency components are not equal, i.e. there are mismatches or inconsistencies between them. The reference frequencies $f_{2A_{\max j}}$ are determined during the initiation by the longitudinal eigenfrequencies f_{Lj} through F_L and the resulting W_f . The noncentral frequencies of F_L are pushed away by the central frequency so that a mismatch between $f_{2A_{\max j}}$ and f_{Lj} is inevitable, as long as there is more than one co-acting longitudinal mode. The vertical eigenfrequencies do not influence the reference frequencies. As vertical modes are independent of longitudinal modes, f_{Nj} and f_{Lj} are usually not equal. Thus, there will usually be mismatches between f_{Nj} , f_{Lj} and $f_{2A_{\max j}}$.

With increasing $2A_{\max}$, the differences in f_{FLij} w.r.t. f_{Lj} increase, as shown in Table 5a, meaning that increasing $2A_{\max}$ disturbs F_L away from its corresponding longitudinal eigenfrequencies f_{Lj} (including the central frequency). The disturbing effects of increasing $2A_{\max}$ are due to the mismatch between the longitudinal and vertical eigenfrequencies.

At the same time, the differences in the f_{FNij} w.r.t. f_{Nj} decrease, as shown in Table 7a. That is, increasing $2A_{\max}$ converges F_N towards its vertical bending eigenfrequencies f_{Nj} , especially for those with small deviations, i.e. small mismatches; see the 987 Hz (0.0% deviation) and 1553 Hz (0.6% deviation) in Figure 7(a). It can also be seen in Figure 7(a) that the differences of f_{FNij} do not converge to 0%, probably due to the mismatches between the reference frequencies and the noncentral longitudinal eigenfrequencies.

Hence, with increasing $2A_{\max}$, the longitudinal vibration is disturbed further away from its initial frequencies, causing weaker F_L (Figure 11(d)), larger W_f and F_L wavelength deviations (Table 2), an increased phase mismatch between the differential wear and the existing corrugation, and a lower wear rate (Figure 10(b)), until the phase of the wear is turned to the opposite of the initial wear (Figure 10(a)), so that the differential wear is in phase with the corrugation, the effect of which erases the corrugation.

6.4. Near-resonance matters

From Figure 10(b), in addition to the longitudinal central wavelength of 28.6 mm, the other three co-acting components also initiate and grow, especially the two that are close to the central frequency, as near-resonance takes place there. This means that exact resonance is not required for corrugation to initiate and grow, and near-resonance can also cause corrugation initiation and growth. In Table 9, the longitudinal eigenfrequency differences of frequency f_j w.r.t. the longitudinal central frequency f_{Lc}

$$|(f_{Lj} - f_{Lc})/f_{Lc}| \quad (5)$$

are 25%, 13% and 14% for the 3 non-central longitudinal frequencies. These differences are converted into the frequency ratio as follows:

$$|(f_{Lc} - f_{Lj})/f_{Lj}| \quad (6)$$

Table 10. The largest relative deviations and differences of W_f , F_L and F_N w.r.t. the frequency.

Reference wavelength (mm)		39.4	33.3	28.6	24.9
Reference frequency (Hz)		987	1168	1360	1562
Longitudinal eigenfrequency (Hz) (& deviation, from Table 4)		1025 (3.9%)	1187 (1.6%)	1360 (0.0%)	1546 (1.0%)
Vertical eigenfrequency (Hz) (& deviation, from Table 6)		987 (0.0%)	1117 (4.4%)	Missing (100%)	1553 (0.6%)
Largest relative deviation (Table 3) or Difference (Tables 7 & 9) of W_f , F_L and F_N	Table 3 ³	8.6%	7.3%	3.1%	0.8%
	Table 5a	7.4%	6.7%	3.2%	1.9%
	Table 5b	11%	7.2%	1.9%	1.0%
	Table 7a	4.9%	15%	–	1.8%
	Table 7b	7.9%	4.9%	–	0.6%

They are 33%, 15%, and 12%. With a 33% frequency ratio, the effect of resonance on corrugation initiation and growth is small, as shown in Figure 10(b), with a 39.4 mm wavelength component (987 Hz). Alternatively, with a 12–15% frequency ratio, the effect of resonance is obvious, as shown by the strong PSD of the 24.5 mm and 33.3 mm wavelengths (1562 and 1168 Hz, respectively). Note that this effective frequency ratio also depends on the damping.

6.5. The wavelength consistency is reduced by increasing $2A_{max}$ towards the vertical central wavelength

Thus far, for all 3 quantities that change with $2A_{max}$, i.e. W_f , F_L and F_N , we have analysed the wavelength (frequency) and phase consistency of the individual quantity W_f with increasing $2A_{max}$ and the consistency between any 2 of the 3, as shown with Case 2 of Table 3.

When consistency is checked simultaneously between all 3, as shown in Case 1 of Table 3, it appears that the consistency between the 3 quantities decreases with increasing $2A_{max}$. At $2A_{max} = 10 \mu\text{m}$, most of the 4 components of the 3 quantities are in light green, with only 2 in dark green, indicating good consistency. At $2A_{max} = 40 \mu\text{m}$, the longest wavelength components become inconsistent (in grey) because the deviation of the longest wear component rises to 8.6%. With increasing $2A_{max}$, the number of light green numbers continuously decreases. At $2A_{max} = 160 \mu\text{m}$, there is only one light green number that remains for each of the 3 quantities; that is, the components corresponding to the highest reference frequency 1562 Hz, namely, the shortest wavelength.

This observation, that the wavelength consistency among all 3 A_{max} -dependent quantities W_f , F_L and F_N seems to be reduced towards the shortest wavelength by increasing $2A_{max}$, should be due to the combined effects of pushing and converging. Table 10 shows the largest relative deviations and differences of the 3 quantities in Tables 5 to 9. It can be seen that all the largest deviations and differences of W_f , F_L (Tables 3, 7a,b and 9b) decrease with decreasing wavelength, except those of F_N (data from Table 7a). This can be explained as follows: the longest wavelength components (39.4 mm) are the farthest from the longitudinal central wavelength and thus suffer the most from the pushing effect. The shortest, 24.9 mm, was the closest, suffering the least. Although 28.6 mm is the longitudinal central wavelength and should have the smallest deviation or difference, a vertical mode is lacking in the current case of RPM3 so that with increasing $2A_{max}$, there is no vertical eigenmode to converge with at the central wavelength, but the closest, that is, the shortest wavelength (24.9 mm). From this discussion and taking the propensity for resonance into account, it is inferred that in general, the wavelength consistency would be reduced to converge to the vertical central frequency (wavelength), a vertical eigenfrequency (wavelength) that is (almost) equal to the longitudinal central frequency (wavelength), or the eigen wavelength that is closest to the vertical central wavelength.

Note that in Table 10, the largest deviations of W_f and F_L at the longitudinal central wavelength (28.6 mm) are larger than those at the wavelength of 24.9 mm. This is not in agreement with the

reasoning that the central wavelength should have the smallest deviation. This is because those of the 28.6 mm take place at $2A_{\max} \geq 80 \mu\text{m}$, with which the longitudinal resonance is already substantially weakened by the pushing and disturbing, while the vertical resonance becomes dominant. The missing vertical eigenmode at 28.6 mm then makes the deviation larger than that at 24.9 mm.

6.6. The largest possible corrugation ($2A_{\max}$)_l

We now examine how $(2A_{\max})_l$ is determined in the case of RPM3. Two factors contribute to the limiting value $(2A_{\max})_l$: the dominance of the vertical excitation $2A_{\max}$ and the F_L wavelength splitting. The 2 factors take place simultaneously at $(2A_{\max})_l = 80 \mu\text{m}$; thus, they seem to be coupled. It is not clear how they are coupled and if they are always coupled.

As observed from Figure 10(b), the PSD of the wear W_f is the lowest at approximately $2A_{\max} = 80 \mu\text{m}$ and changes with increasing $2A_{\max}$ from decreasing trend to increasing. This is caused by the continuously increasing influence of the vertical vibration, as shown in the continuously increasing PSD of F_N (Figure 11(c)), the accompanying monotonously decreasing PSD of the 2 groups of shorter F_L wavelength components at approximately 24.9 and 28.6 mm (Figure 11(d)), and the accompanying change in the PSD from decreasing to increasing at $2A_{\max} = 80 \mu\text{m}$ of the 2 longer F_L wavelength components at approximately 33.3 and 39.4 mm. This means that with the current parameter set RPM3, the vertical dominance starts at $(2A_{\max})_l = 80 \mu\text{m}$.

The wavelength splitting also affects F_L at $2A_{\max} = 80 \mu\text{m}$, probably caused by the increased vertical excitation (recall that the longer wavelength component from the splitting has a frequency close to and converging towards the vertical eigenfrequency of 1117 Hz). The splitting sharply further reduces the wavelength consistency between F_L and the longitudinal modes (Table 5a), so that the consistent growth of the corrugation is broken at $(2A_{\max})_l = 80 \mu\text{m}$.

Thus, it is the consistency between the vertical and longitudinal modes and their interplay that determine the value of $(2A_{\max})_l$. Note that wear is the only damage mechanism considered for $(2A_{\max})_l$. Consideration of plastic deformation as a damage mechanism may lead to a different $(2A_{\max})_l$ value.

The above discussion is made with RPM3, with which the vertical bending eigenfrequencies are different from the longitudinal eigenfrequencies. It has been seen that when the respective longitudinal and vertical eigenfrequencies are not equal, deviations will occur between W_f , F_L and F_N , and the consistency tends to converge to the vertical central frequency. On the other hand, if the co-acting longitudinal and vertical eigenfrequencies are 100% equal, then the abovementioned cause of deviations by the disturbing effect is removed. The frequencies of W_f , F_L and F_N can, however, still not have a full match between them, i.e. not be fully consistent, because of the pushing effect of the longitudinal central frequency.

For full consistency among W_f , F_L and F_N , the only possibility seems to be that there is only one eigenmode for longitudinal compression and one for vertical bending. Their frequencies are equal and are the longitudinal and vertical central frequencies. In this case, the pushing and disturbing effects will disappear, and a converging effect is not needed. It seems then that $(2A_{\max})_l$ would be infinite. That is, however, impossible due to possible wavelength splitting because of the following: 1) a large $2A_{\max}$ tends to favour the growth of a large wavelength, 2) a large dynamic contact force due to the large corrugation amplitude will cause damage and thus changes to the track and fastening so the RPM3 condition does not hold anymore, and 3) with a large dynamic contact force, the damage mechanism will no longer be pure wear.

The discussion thus far has shown that corrugation initiates without vertical bending and can grow until $(2A_{\max})_l = 80 \mu\text{m}$, where vertical bending dominates. This can explain why corrugation can form on continuously supported tracks where pinned-pinned resonance does not exist [15,22].

6.7. Mechanism of frequency selection and speed independence

It is seen from the discussion thus far that it is the longitudinal and vertical vibration modes, as well as the competition between them, that determine the overall wavelength and the $(2A_{\max})_l$.

We now see how the overall wavelength is determined. We assume that there are multiple wavelengths that co-act. In the case with RPM3, there is a central frequency at the longitudinal mode (1360 Hz) where exact resonance takes place with the traffic speed $v = 140$ km/h. This mode has the strongest PSD of W_f and thus grows the fastest until $2A_{\max} = 40 \mu\text{m}$ (see Figure 10(b)). Then, it can be said that the (longitudinal) central frequency f_{Lc} of the corrugation is ‘selected’ to be the 1360 Hz eigenfrequency by the initial excitation and the traffic speed v , with the corresponding central wavelength $\lambda_c = 28.6$ mm following from $\lambda_c = v/f_{Lc}$.

What can be expected to happen if the traffic speed changes? Suppose the traffic speed is $v = 91.9$ km/h; this should cause exact resonance at the longitudinal eigenfrequency of 1025 Hz. It means that the longitudinal central frequency will jump from 1360 Hz to 1025 Hz with the corresponding wavelength being 24.9 mm. If $v = 219$ km/h, then the corresponding (longitudinal central) frequency and wavelength will be 1546 and 39.4 mm, respectively. Thus, when the traffic speed is varied from 91.9 to 219 km/h, the central wavelength component varies from 24.9 mm to 39.4 mm. The ratio of the speed range $219/91.9 = 2.38$ is much larger than that of the wavelength range $39.4/24.9 = 1.58$.

The next question is: what can be expected to happen if the traffic speed does not exactly correspond to a central wavelength? Since near resonance also causes corrugation initiation and growth, it is expected that if a speed can cause near-resonance, then corrugation should also initiate and grow. For example, if $v = 180$ km/h, 2 scenarios can be considered: (1) There is no corrugation yet, i.e. $2A_{\max} = 0 \mu\text{m}$. Divide this speed with the 4 longitudinal eigenfrequencies of 1025, 1187, 1360 and 1546 Hz, and the resulting wavelengths are 48.8, 42.1, 36.8 and 32.3 mm, all of which are within the 20–80 mm range of short pitch corrugation. If we limit the discussion to the range discussed thus far of 24.9 ~ 39.4 mm of RPM3, then the longitudinal central frequency would be 1360 or 1546 Hz, corresponding to the wavelengths 36.8 mm and 32.3 mm, which should co-act and with which corrugation is expected to initiate and grow. (2) Initial corrugation is already present with, e.g. $2A_{\max} = 10 \mu\text{m}$, like the one shown in Figure 10 and Table 2. The wheel rolling over the corrugation will induce passing frequencies of 1269, 1501, 1748 and 2008 Hz, which correspond to the 4 reference wavelengths. The frequencies 1269 and 1501 Hz are between the longitudinal eigenfrequencies of 1187, 1360 and 1546 Hz. The ratios of the passing frequencies over the longitudinal eigenfrequencies are shown in Table 11; 4 of the 6 ratios are not larger than 10% and hence are smaller than the 12–15% frequency ratio of the 24.9 mm and 33.3 mm wavelengths above. Thus, effective near-resonance may occur at the 3 eigenfrequencies, and the 3 corresponding wavelength components of 24.9, 28.6 and 33.3 mm should grow.

A similar conclusion can be made with other speeds. Thus, corrugation can, with RPM3, initiate and grow between 91.9 and 219 km/h.

If lower or higher longitudinal eigenfrequencies, including the fundamental frequencies and harmonics of the system, are considered, then this speed range can be further extended. For example, there is a strong PSD at 63.6 mm wavelength in Figure 7(b); this corresponds to a longitudinal compression mode of 611 Hz with $v = 140$ km/h. With $v = 54.8$ km/h, resonance at this eigenfrequency could be induced with a wavelength of 24.9 mm. Thus, with this eigenmode, the speed range of RPM3 is extended from 91.9 ~ 219 km/h to 54.8 ~ 219 km/h, in which corrugation can initiate and grow with a central wavelength between 24.9–39.4 mm. The ratio of the speed range

Table 11. Ratio of the passing frequency over the longitudinal eigenfrequency.

Longitudinal eigenfrequency (Hz)	1187	1360	1546
Passing frequency 1269 Hz	6.9%	6.7%	18%
Passing frequency 1501 Hz	26%	10%	2.9%

is $219/54.8 = 4.00$, with the ratio of the wavelength range remaining at 1.58. In this way, the traffic speed can vary in a large range while the apparent overall wavelength remains seemingly unchanged, or, in other words, ‘fixed.’

This hypothesis explains why the overall wavelength of corrugation is not linearly proportional to the traffic speed if the wavelength is determined by the eigenfrequencies. It is a mechanism of frequency selection that fixes the apparent overall wavelength of short pitch corrugation around a certain value or in a small range, seemingly independent of traffic speed. This may help explain the field data about the small variation between the corrugation wavelength and train speed [1,15].

The hypothesized formation mechanism is summarized as follows: A longitudinal central eigenfrequency is selected from the longitudinal compression eigenfrequency by resonance with the passing traffic speed; resonance takes place at the central frequency to generate the different wear and the consequential corrugation. When the traffic speed changes, near-resonance occurs at the central frequency, or the central frequency jumps to another longitudinal eigenfrequency to maintain (near-) resonance. By this, the apparent overall wavelength of the corrugation is ‘fixed’ in a narrow range that is not linearly proportional to the change in the traffic speed, showing an seemingly apparent independency of the wavelength on the speed. The mechanism is in essence frequency selection, instead of wavelength selection. In future research, the effect of different running speeds on corrugation wavelength will be further examined employing the 3D FE model.

7. Conclusions and further work

Utilizing a 3D FE approach that is proven to be effective in modelling wheel-track interactions by simultaneously considering the contact mechanics and the structural dynamics, as well as their interplay, this paper examines the conditions for consistent initiation and growth of short pitch corrugation by simulating a hypothesized corrugation formation process. Being consistent means that the differential wear due to a sequence of wheel-rail contact adds up so that the corrugation continuously grows. The hypothesis is shown to hold, and the corrugation formation process works as follows:

- (1) The longitudinal compression eigenmodes, instead of the vertical bending eigenmodes, determine corrugation initiation, as inferred in [26]. Consequently, an initial excitation that allows flexibility for longitudinal modes to vibrate is needed for the initiation.
- (2) A type of effective initial excitation is fastening RPM3 and RPM4, which, together with the overall wheel-track system, generate eigenmodes that can potentially resonate with the traffic and allow flexibility for longitudinal resonance to produce significant wear for corrugation initiation and growth. Allowing flexibility for the vertical vibration modes with strong longitudinal constraints did not give rise to corrugation initiation, which could explain the corrugation-free track that is commonly observed in the field. Lateral vibration modes with the fastening constraints RPM1 ~ 5 and with rail inclination up to 1/40 did not contribute to corrugation initiation.
- (3) The central wavelength λ_c of the initial corrugation is determined by resonance of a longitudinal eigenfrequency with the passing speed v of the wheels according to $\lambda_c = v/f_{Lc}$. Multiple eigenfrequencies may co-act around the central frequency f_{Lc} , causing multiple components of differential wear by near-resonance, contributing to the overall apparent wavelength of the corrugation, which is the superposition of the multiple wavelength components, including the central component.
- (4) Once initial corrugation exists, this corrugation induces vertical vibration, causing differential wear that superposes on the wear by the initial excitation. The strength of this vibration increases with the corrugation amplitude.

- (5) The initial excitation can induce significant longitudinal vibration only, and the longitudinal vibration has negligible direct influence on the vertical vibration. Vertical excitation can induce significant longitudinal vibration and much stronger vertical vibration.
- (6) Whether or not this corrugation under the simultaneous action of the initial excitation and the excitation by the corrugation grows depends on the following:
 - (a) The consistency between the longitudinal and vertical eigenmodes that co-act and produce their respective wear components. Vertical modes that can (near-) resonate with the (initial) corrugation promote growth.
 - (b) The relative strength of the longitudinal and vertical vibrations. Initially, the vertical excitation is null or weak; thus, the initial excitation dominates the growth. With increasing corrugation amplitude, the vertical excitation becomes stronger and gradually takes over the dominance.
 - (c) This consistency and this relative strength determine the maximum corrugation amplitude $(2A_{\max})_l$. For RPM3, this $(2A_{\max})_l$ is 80 μm , for which wear is considered the only damage mechanism.
- (7) Consistency is needed not only between longitudinal and vertical modes but also between the longitudinal modes and between the vertical modes, as the different modes cause different wavelength components in the differential wear and thus in the apparent overall corrugation.
 - (a) When multiple longitudinal eigenmodes contribute to the (initial) corrugation, the near-resonance at the non-central modes is pushed away from their eigenfrequencies by the resonance at the central frequency. The farther a mode is away from the central mode, the less contribution it makes to the corrugation, and the lower consistency it has with the central corrugation component.
 - (b) Existing corrugation as a vertical excitation disturbs the differential wear away from their wavelengths determined by the longitudinal modes and converges the corrugation towards the vertical central wavelength if the frequencies of the vertical and longitudinal modes are different. This disturbing and converging will not occur only if there is one longitudinal mode and one vertical mode that contribute to the corrugation, and the frequencies of the two modes are equal and are the central frequencies.
 - (c) The disturbing and pushing effects increase the inconsistency of the noncentral components. They confine resonance to a few co-acting longitudinal and vertical modes that are within an approximately 15% frequency ratio around the longitudinal central frequency. They make the central component of the corrugation increasingly dominant with increasing corrugation amplitude if the traffic speed is constant.
 - (d) A large corrugation amplitude can cause frequency splitting, which can significantly affect the consistency.
- (8) The corrugation develops by frequency selection instead of wavelength fixing. The formation mechanism works as follows: A longitudinal central eigenfrequency is selected from the longitudinal compression eigenfrequencies by resonance with passing traffic speed; resonance takes place at or around the central frequency to generate the differential wear and the consequential corrugation. Near-resonance can occur around the central frequency if there is a small speed change. Alternatively, the central frequency can jump to another longitudinal eigenfrequency in a large frequency range to maintain the maximum (near-) resonance in response to a large change in the traffic speed. By this, the apparent overall wavelength of the corrugation seems to be 'fixed' because it changes only in a narrow range that is not proportional to the large change in the traffic speed, showing a seemingly apparent independency of the wavelength on the speed. When the corrugation amplitude is large enough, vertical excitation and vertical eigenmodes come into play through the necessary consistency, as summarized above.

The simulated results are based on the typical parameters of the railway in the Netherlands and agree with field observations such as the wavelength and periodicity of corrugation. The corrugation formation mechanism can explain why corrugation forms on continuously supported tracks where pinned-pinned resonance does not exist. It may help explain the field data with respect to the small variation between the corrugation wavelength and train speed.

The initial excitation considered in this work is in general a state of rail fastenings determined by design, construction, degradation and maintenance. Without an effective initial excitation, corrugation cannot initiate and grow. It should be noted that rail fastenings may not be the only effective initial excitation for corrugation formation. Other conditions that can effectively excite eigenmodes of vehicle-track system, induce dynamic wheel-rail contact force, and cause differential wear, may also lead to corrugation consistent development. Further work will include experimental verification of the formation mechanism in laboratory-controlled conditions, as well as design of fastenings that can better prevent or reduce corrugation by construction and maintenance. Frequency splitting is found to play an important role in changing the consistency. It may be interesting to investigate methods that can induce such splitting at an earlier stage to stop the consistent growth of corrugation.

Notes

1. RPM is abbreviation of RailPad Model. RPM is used instead of FM (Fastening model) to avoid confusion with FE or FEM.
2. Here we do not distinguish between vertical and normal contact forces because the corrugation takes place in the middle of rail top, where the difference between the normal and vertical directions is by the rail inclination and is small. The influence of this difference is examined in [Section 4.4.4](#).
3. Excluding the case $2A_{\max} = 0$, which does not include the influence of $2A_{\max}$ so that the consistency between its F_N and the other 2 quantities is irrelevant.

Acknowledgements

This research was partly supported by ProRail and by NeTIRail-INFRA, an EU Horizon 2020 programme for research and innovation (project No. 636237).

Disclosure statement

No potential conflict of interest was reported by the author(s).

Funding

The work was supported by the European Commission [636237]

References

- [1] Grassie S, Kalousek J. Rail corrugation: characteristics, causes and treatments. *Proc Inst Mech Eng F J Rail Rapid Transit*. 1993;207(1):57–68.
- [2] Suda Y, Komine H, Iwasa T, et al. Experimental study on mechanism of rail corrugation using corrugation simulator. *Wear*. 2002;253(1–2):162–171.
- [3] Jin X, Wen Z. Rail corrugation formation studied with a full-scale test facility and numerical analysis. *Proc Inst Mech Eng J*. 2007;221(6):675–698.
- [4] Bellette P, Meehan P, Daniel W. Validation of a tangent track corrugation model with a two disk test rig. *Wear*. 2011;271(1–2):268–277.
- [5] Li W, Wang H, Wen Z, et al. An investigation into the mechanism of metro rail corrugation using experimental and theoretical methods. *Proc Inst Mech Eng F J Rail Rapid Transit*. 2016;230(4):1025–1039.
- [6] Liu Q, Zhang B, Zhou Z. An experimental study of rail corrugation. *Wear*. 2003;255(7–12):1121–1126.
- [7] Feller H, Walf K. Surface analysis of corrugated rail treads. *Wear*. 1991;144(1–2):153–161.

- [8] Wild E, Wang L, Hasse B, et al. Microstructure alterations at the surface of a heavily corrugated rail with strong ripple formation. *Wear*. 2003;254(9):876–883.
- [9] Saulot A, Descartes S, Desmyter D, et al. A tribological characterization of the “damage mechanism” of low rail corrugation on sharp curved track. *Wear*. 2006;260(9–10):984–995.
- [10] Zhang HW, Ohsaki S, Mitao S, et al. Microstructural investigation of white etching layer on pearlite steel rail. *Mater Sci Eng A*. 2006;421(1–2):191–199.
- [11] Zhang H, Zhang S, Zhong H, et al. Damage mechanism of a long-wavelength corrugated rail associated with rolling contact fatigue. *Eng Fail Anal*. 2022;136:106173.
- [12] Muller S. A linear wheel–track model to predict instability and short pitch corrugation. *J Sound Vibr*. 1999;227(5):899–913.
- [13] Nielsen J. Numerical prediction of rail roughness growth on tangent railway tracks. *J Sound Vibr*. 2003;267(3):537–548.
- [14] Wu T, Thompson D. An investigation into rail corrugation due to micro-slip under multiple wheel/rail interactions. *Wear*. 2005;258(7–8):1115–1125.
- [15] Afferrante L, Ciavarella M. Short-pitch rail corrugation: a possible resonance-free regime as a step forward to explain the “enigma”? *Wear*. 2009;266(9–10):934–944.
- [16] Baeza L, Vila P, Xie G, et al. Prediction of rail corrugation using a rotating flexible wheelset coupled with a flexible track model and a non-Hertzian/non-steady contact model. *J Sound Vibr*. 2011;330(18–19):4493–4507.
- [17] Cui X, Chen G, Yang H, et al. Study on rail corrugation of a metro tangential track with Cologne-egg type fasteners. *Veh Syst Dyn*. 2016;54(3):353–369.
- [18] Cui X, Chen G, Zhao J, et al. Field investigation and numerical study of the rail corrugation caused by frictional self-excited vibration. *Wear*. 2017;376–377:1919–1929.
- [19] Fourie D, Fröhling R, Heyns S. Railhead corrugation resulting from mode-coupling instability in the presence of veering modes. *Tribol Int*. 2020;152:106499.
- [20] Ma C, Gao L, Xin T, et al. The dynamic resonance under multiple flexible wheelset-rail interactions and its influence on rail corrugation for high-speed railway. *J Sound Vibr*. 2021;498:115968.
- [21] Sato Y, Matsumoto A, Knothe K. Review on rail corrugation studies. *Wear*. 2002;253(1–2):130–139.
- [22] Oostermeijer K. Review on short pitch rail corrugation studies. *Wear*. 2008;265(9–10):1231–1237.
- [23] Han J, Xiao X, Wu Y, et al. Effect of rail corrugation on metro interior noise and its control. *Appl Acoust*. 2018;130:63–70.
- [24] Xin T, Wang S, Gao L, et al. Field measurement of rail corrugation influence on environmental noise and vibration: a case study in China. *Measurement*. 2020;164:108084.
- [25] Kalousek J, Johnson K. An investigation of short pitch wheel and rail corrugations on the vancouver mass transit system. *Proc Inst Mech Eng F J Rail Rapid Transit*. 1992;206(2):127–135.
- [26] Li S, Li Z, Núñez A, et al. New insights into the short pitch corrugation enigma based on 3D-FE coupled dynamic vehicle-track modeling of frictional rolling contact. *Appl Sci*. 2017;7(8):807.
- [27] Grassie S. Rail corrugation: characteristics, causes, and treatments. *Proc Inst Mech Eng F J Rail Rapid Transit*. 2009;223(6):581–596.
- [28] Knothe K, Groß-Thebing A. Short wavelength rail corrugation and non-steady-state contact mechanics. *Veh Syst Dyn*. 2008;46(1–2):49–66.
- [29] Zhao X, Zhang P, Wen Z. On the coupling of the vertical, lateral and longitudinal wheel-rail interactions at high frequencies and the resulting irregular wear. *Wear*. 2019;430:317–326.
- [30] Santa J, Toro A, Lewis R. Correlations between rail wear rates and operating conditions in a commercial railroad. *Tribol Int*. 2016;95:5–12.
- [31] Vuong T, Meehan P, Eadie D, et al. Investigation of a transitional wear model for wear and wear-type rail corrugation prediction. *Wear*. 2011;271(1–2):287–298.
- [32] Meehan P, Bellette P, Batten R, et al. A case study of wear-type rail corrugation prediction and control using speed variation. *J Sound Vibr*. 2009;325(1–2):85–105.
- [33] Neilsen J. Evolution of rail corrugation predicted with a non-linear wear model. *J Sound Vibr*. 1999;227(5):915–933.
- [34] Chen G, Zhou Z, Ouyang H-J, et al. A finite element study on rail corrugation based on saturated creep force-induced self-excited vibration of a wheelset–track system. *J Sound Vibr*. 2010;329(22):4643–4655.
- [35] Chen G, Cui X, Qian W. Investigation into rail corrugation in high-speed railway tracks from the viewpoint of the frictional self-excited vibration of a wheel–rail system. *J Mod Transp*. 2016;24(2):124–131.
- [36] Sun YQ, Simson S. Wagon–track modelling and parametric study on rail corrugation initiation due to wheel stick-slip process on curved track. *Wear*. 2008;265(9–10):1193–1201.
- [37] Hory C, Bouillault L, Aknin P. Time–frequency characterization of rail corrugation under a combined auto-regressive and matched filter scheme. *Mech Syst Signal Process*. 2012;29:174–186.
- [38] Jin X, Wen Z. Effect of discrete track support by sleepers on rail corrugation at a curved track. *J Sound Vibr*. 2008;315(1–2):279–300.

- [39] Wu T. Parametric excitation of wheel/track system and its effects on rail corrugation. *Wear*. 2008;265(9–10):1176–1182.
- [40] Tassilly E, Vincent N. Rail corrugations: analytical model and field tests. *Wear*. 1991;144(1–2):163–178.
- [41] Correa N, Vadillo E, Santamaria J, et al. A versatile method in the space domain to study short-wave rail undulatory wear caused by rail surface defects. *Wear*. 2016;352:196–208.
- [42] Grassie SL. Rail corrugation: advances in measurement, understanding and treatment. *Wear*. 2005;258(7–8):1224–1234.
- [43] Yang Z, Zhang P, Wang L. Wheel-rail impact at an insulated rail joint in an embedded rail system. *Eng Struct*. 2021;246:113026.
- [44] Remington PJ. Wheel/Rail noise—part IV: rolling noise. *J Sound Vibr*. 1976;46(3):419–436.
- [45] Escalona JL, Aceituno JF. Multibody simulation of railway vehicles with contact lookup tables. *Int J Mech Sci*. 2019;155:571–582.
- [46] Yu X, Aceituno JF, Kurvinen E, et al. Comparison of numerical and computational aspects between two constraint-based contact methods in the description of wheel/rail contacts. *Multibody Sys Dyn*. 2022;54(3):303–344.
- [47] Shen C, Deng X, Wei Z, et al. Comparisons between beam and continuum models for modelling wheel-rail impact at a singular rail surface defect. *Int J Mech Sci*. 2021;198:106400.
- [48] Xu L, Chen X, Li X, et al. Development of a railway wagon-track interaction model: case studies on excited tracks. *Mech Syst Signal Process*. 2018;100:877–898.
- [49] Dimitrová Z. Two-layer model of the railway track: analysis of the critical velocity and instability of two moving proximate masses. *Int J Mech Sci*. 2022;217:107042.
- [50] Yang Z, Boogaard A, Wei Z, et al. Numerical study of wheel-rail impact contact solutions at an insulated rail joint. *Int J Mech Sci*. 2018;138:310–322.
- [51] Xu J, Wang K, Liang X, et al. Influence of viscoelastic mechanical properties of rail pads on wheel and corrugated rail rolling contact at high speeds. *Tribol Int*. 2020;151:106523.
- [52] Xie G, Iwnicki SD. Simulation of wear on a rough rail using a time-domain wheel-track interaction model. *Wear*. 2008;265(11–12):1572–1583.
- [53] Zhao X, Huang S, Zhang P, et al. On the modelling of normal wheel-rail contact for high-frequency vehicle-track dynamics analyses. *Int J Rail Trans*. 2021;10(6):1–22.
- [54] Jin X, Wen Z, Wang K. Effect of track irregularities on initiation and evolution of rail corrugation. *J Sound Vibr*. 2005;285(1–2):121–148.
- [55] Li Z, Dollevoet R, Molodova M, et al. Squat growth—some observations and the validation of numerical predictions. *Wear*. 2011;271(1–2):148–157.
- [56] Deng X, Qian Z, Li Z, et al. Investigation of the formation of corrugation-induced rail squats based on extensive field monitoring. *Int J Fatigue*. 2018;112:94–105.
- [57] Li Z, Zhao X, Dollevoet R, et al. Differential wear and plastic deformation as causes of squat at track local stiffness change combined with other track short defects. *Veh Syst Dyn*. 2008;46(sup1):237–246.
- [58] Jin X, Wen Z, Wang K, et al. Effect of a scratch on curved rail on initiation and evolution of rail corrugation. *Tribol Int*. 2004;37(5):385–394.
- [59] Deng X, Li Z, Qian Z, et al. Pre-cracking development of weld-induced squats due to plastic deformation: five-year field monitoring and numerical analysis. *Int J Fatigue*. 2019;127:431–444.
- [60] Egana J, Vinolas J, Seco M. Investigation of the influence of rail pad stiffness on rail corrugation on a transit system. *Wear*. 2006;261(2):216–224.
- [61] Ilias H. The influence of railpad stiffness on wheelset/track interaction and corrugation growth. *J Sound Vibr*. 1999;227(5):935–948.
- [62] Zhao X, Li Z. The solution of frictional wheel-rail rolling contact with a 3D transient finite element model: validation and error analysis. *Wear*. 2011;271(1–2):444–452.
- [63] Yang Z, Deng X, Li Z. Numerical modeling of dynamic frictional rolling contact with an explicit finite element method. *Tribol Int*. 2019;129:214–231.
- [64] Knothe K, Grassie S. Modelling of railway track and vehicle/track interaction at high frequencies. *Veh Syst Dyn*. 1993;22(3–4):209–262.
- [65] Wu Y, Du X, Zhang H-J, et al. Experimental analysis of the mechanism of high-order polygonal wear of wheels of a high-speed train. *J Zhejiang Univ Sci A*. 2017;18:579–592.
- [66] Li Z, Zhao X, Esveld C, et al. An investigation into the causes of squats—correlation analysis and numerical modeling. *Wear*. 2008;265(9–10):1349–1355.
- [67] Benson DJ, Hallquist JO. A single surface contact algorithm for the post-buckling analysis of shell structures. *Comput Methods Appl Mech Eng*. 1990;78(2):141–163.
- [68] Courant R, Friedrichs K, Lewy H. On the partial difference equations of mathematical physics. *IBM J Res Dev*. 1967;11(2):215–234.
- [69] Wei Z, Li Z, Qian Z, et al. 3D FE modelling and validation of frictional contact with partial slip in compression-shift-rolling evolution. *Int J Rail Trans*. 2016;4(1):20–36.

- [70] Oregui M, Li Z, Dollevoet R. An investigation into the vertical dynamics of tracks with monoblock sleepers with a 3D finite-element model. *Proc Inst Mech Eng F J Rail Rapid Transit.* 2016;230(3):891–908.
- [71] Molodova M, Li Z, Núñez A, et al. Validation of a finite element model for axle box acceleration at squats in the high frequency range. *Comput Struct.* 2014;141:84–93.
- [72] Li Z, Zhao X, Dollevoet R. An approach to determine a critical size for rolling contact fatigue initiating from rail surface defects. *Int J Rail Trans.* 2017;5(1):16–37.
- [73] Grassie S. Squats and squat-type defects in rails: the understanding to date. *Proc Inst Mech Eng F J Rail Rapid Transit.* 2012;226(3):235–242.
- [74] Zhao X, Li Z, Dollevoet R. Influence of the fastening modeling on the vehicle-track interaction at singular rail surface defects. *J Comput Nonlin Dyn.* 2014;9(3). DOI:10.1115/1.4025895
- [75] Hempelmann K, Knothe K. An extended linear model for the prediction of short pitch corrugation. *Wear.* 1996;191(1–2):161–169.
- [76] Zhang P, Li S, Núñez A, et al. Vibration modes and wave propagation of the rail under fastening constraint. *Mech Syst Signal Process.* 2021;160:107933.
- [77] Zhang P, Moraal J, Li Z. Design, calibration and validation of a wheel-rail contact force measurement system in V-track. *Measurement.* 2021;175:109105.
- [78] Ewins DJ. The effects of detuning upon the forced vibrations of bladed disks. *J Sound Vibr.* 1969;9(1):65–79.